Final Draft
of the original manuscript:

Le, T.; Pistidda, C.; Puszkiel, J.; Castro Riglos, M.; Karimi, F.; Skibsted, J.; Payandeh GharibDoust, S.; Richter, B.; Emmler, T.; Milanese, C.; Santoru, A.; Hoell, A.; Krumrey, M.; Gericke, E.; Akiba, E.; Jensen, T.; Klassen, T.; Dornheim, M.:

Design of a Nanometric AlTi Additive for MgB2-Based Reactive Hydride Composites with Superior Kinetic Properties

In: The Journal of Physical Chemistry C. Vol. 122 (14), 2018, 7642 - 7655.
First published online by ACS: 21.03.2018

DOI: 10.1021/acs.jpcc.8b01850
https://dx.doi.org/10.1021/acs.jpcc.8b01850

Design of a Nanometric AlTi Additive for MgB_2 Based Reactive Hydride Composites with Superior Kinetic Properties

Thi-Thu Le[a], Claudio Pistidda[a,], Julián Puszkiel[a,b], María Victoria Castro Riglos[a,c], Fahim Karimi[a], Jørgen Skibsted[d], SeyedHosein Payandeh GharibDoust[d], Bo Richter[d], Thomas Emmler[a], Chiara Milanese[e], Antonio Santoru[a], Armin Hoell[f], Michael Krumrey[g], Eike Gericke[h], Etsuo Akiba[i], Torben R. Jensen[d], Thomas Klassen[a,j], Martin Dornheim[a]*

[a]Institute of Materials Research, Materials Technology, Helmholtz-Zentrum Geesthacht GmbH, Max-Planck Straße 1, D-21502 Geesthacht, Schleswig-Holstein, Germany

[b]Department of Physicochemistry of Materials, Consejo Nacional de Investigaciones Científicasy Técnicas (CONICET) and Centro Atómico Bariloche, Av. Bustillo km 9500 S.C. de Beriloche, Argentina.

[c]Department of Metalphysics, Consejo Nacional de Investigaciones Científicas y Técnicas (CONICET) and Centro Atómico Bariloche, Av. Bustillo km 9500 S.C. de Bariloche, Argentina

[d]Department of Chemistry and Interdisciplinary Nanoscience Center (iNANO), Aarhus University, Langelandsgade 140, 8000 Aarhus C, Denmark

[e]Pavia H_2 Lab, C.S.G.I. & Department of Chemistry, Physical Chemistry Section, University of Pavia, Italy

[f]Institute for Nanospectroscopy, Helmholtz-Zentrum Berlin für Materialien und Energie, Albert-Einstein-Strasse 15, Berlin, Germany

[g]Physikalisch-Technische Bundesanstalt (PTB), Abbestraße 2-12, 10587 Berlin, Germany

[h]Humboldt-Universität zu Berlin, Institut für Chemie, Brook-Taylor Straße 2, Berlin, Germany

[i]Department of Mechanical Engineering, Kyushu University, 744 Motooka Nishi-ku Fukuoka 819-0395, Japan

[j]Helmut Schmidt University, Holstenhofweg 85, 22043 Hamburg, Germany

ABSTRACT

Solid-state hydride compounds are a promising option for efficient and safe hydrogen storage systems. Lithium reactive hydride composite system $2LiBH_4+MgH_2/2LiH+MgB_2$ (Li-RHC) has been widely investigated owing to its high theoretical hydrogen storage capacity and low calculated reaction enthalpy (11.5 wt.% H_2 and 45.9 kJ/mol H_2). In this paper, a thorough investigation into the effect of the formation of nano TiAl alloys on the hydrogen storage properties of the Li-RHC is presented. The additive $3TiCl_3.AlCl_3$ is used as nanoparticle precursor. For the investigated temperatures and hydrogen pressures, the addition of ~ 5 wt. % of $3TiCl_3.AlCl_3$ leads to hydrogenation/dehydrogenation times of only 30 min and to a reversible hydrogen storage capacity of 9.5 wt.%. The material containing $3TiCl_3.AlCl_3$ possesses superior hydrogen storage properties in terms of rates and stable hydrogen capacity during several hydrogenation/dehydrogenation cycles. These enhancements are attributed to an *in situ* nanostructure and hexagonal $AlTi_3$ phase observed by HR-TEM. This phase acts in a twofold manner, first promoting the nucleation of MgB_2 upon dehydrogenation and second suppressing the formation of $Li_2B_{12}H_{12}$ upon hydrogenation/dehydrogenation cycling.

1. INTRODUCTION

Hydrogen is widely recognized as a promising energy carrier for a clean and environmental friendly energy. Nowadays, hydrogen is commonly stored in liquid or compressed gas form[1-3]. However, both storage methods are neither safe nor cost efficient. Hydrogen can also be stored in solid state: this is the safest solution to store it since mainly the pressure and temperature conditions are milder than those required for the compressed and cryogenic hydrogen storage methods, respectively. Because of their high volumetric hydrogen storage capacities, light metal complex hydrides are considered potential storage candidates for hydrogen driven applications[4,5]. Among the complex metal hydrides, $LiBH_4$ possesses one of the highest gravimetric and volumetric hydrogen storage capacities (18.5 wt.% H_2 and 121 kg H_2/m^3, respectively)[6-8]. However, the dehydrogenation of $LiBH_4$ takes place only at relatively high temperatures (over 400 °C) and its decomposition products (i.e. LiH, B, $Li_2B_{12}H_{12}$) are too stable to reversibly form $LiBH_4$ under moderate temperature and hydrogen pressure[9-14]. Barkhordarian *et al.*[15] and Vajo *et al.*[16] independently reported on the possibility to obtain fully reversible metal borohydrides based hydrogen storage systems. Owing to its theoretical hydrogen storage capacity and calculated reaction enthalpy (11.5 wt.% H_2 and 45.9 kJ/mol H_2), the $2LiBH_4+MgH_2/2LiH+MgB_2$ (Li-RHC) system is regarded as one of the most prominent candidates for hydrogen storage. However, the dehydrogenation andhydrogenation processes of this composite system take place only at relative elevated temperatures (over 350 °C) due to kinetic constraints. Under dynamic conditions the dehydrogenation reaction occurs in a steps reaction: $2LiBH_{4(l)} + MgH_{2(s)} \rightarrow Mg_{(s)} + 2LiBH_{4(l)} + H_{2(g)} \rightarrow 2LiH_{(s)} + MgB_{2(s)} + 4H_{2(g)}$ [17]. Additionally, as also observed in other RHC systems[18-22], the Li-RHC system reacts *via* different pathways depending on the temperature and pressure conditions and requires an appropriate hydrogen overpressure during the dynamic

dehydrogenation process to assure the reversibility of the hydrogen uptake-release process[23,24]. In the last decade, several studies have been conducted to investigate the effect of transition metal (TM) based additives (*e.g.* Ti containing additives, Zr containing additives, V containing additives, Sc_2O_3, Nb_2O_5, NbF_5 and Ce containing additives) on the dehydrogenation/hydrogenation reaction rates of $2LiBH_4+MgH_2$. In addition, some attempts to improve the reaction kinetics of $2LiBH_4+MgH_2$ by doping it with metallic Al were also taken[25-34]. Among the transition metal additives, the Li-RHC doped with 5 mol % $TiCl_3$ shows markedly improved kinetic behavior. Bösenberg *et al.*[25] reported that the addition of TM or TM-compounds improve the kinetic behavior of Li-RHC by forming transition metal borides that provide heterogeneous nucleation sites for the formation of MgB_2 upon desorption .

In the present work, the effects of the *in situ* formation of nano AlTi alloys on the hydrogen storage properties of the Li-RHC system are thoroughly investigated. For comparison purposes, the hydrogenation and dehydrogenation properties of the Li-RHC+$3TiCl_3.AlCl_3$ system are compared with the ones of the pristine Li-RHC and Li-RHC+$TiCl_3$ systems. The dehydrogenation and hydrogenation kinetic behavior are evaluated by volumetric and calorimetric techniques. The hydride systems are further characterized by means of *in situ* synchrotron powder X-ray diffraction, Magic Angle Spinning Solid-state Nuclear Magnetic Resonance, High resolution Transmission Electron Microscopy and Anomalous Small-Angle X-ray Scattering methods.

2. EXPERIMENTAL SECTION

2.1. Sample preparation

The raw materials were purchased in powder form from commercial suppliers without further modification: Lithium borohydride ($LiBH_4$, 95 % purity, Sigma Aldrich), magnesium hydride

(MgH_2, 98 % purity, Alfa Aesar), lithium hydride (LiH, 95 % purity, Sigma Aldrich), magnesium boride (MgB_2, 99 % purity, Alfa Aesar), titanium (III) chloride ($TiCl_3$, 99.999% purity, Alfa Aesar) and aluminum (III) chloride-titanium (III) chloride ($3TiCl_3.AlCl_3$, ~ 76-78% $TiCl_3$ purity, Fisher Scientific). The $2LiBH_4+MgH_2$ (Li-RHC_a) and $2LiH+MgB_2$ (Li-RHC_d) systems were mixed in several different ratios with $TiCl_3$ and $3TiCl_3.AlCl_3$ (Li-RHC_a +*x*A and Li-RHC_d +*x*A, *x*= from 0.3125 to 2.5 mol %; A= $TiCl_3$ or $3TiCl_3.AlCl_3$). In order to obtain a homogeneous dispersion of the additives into the main hydride phases, all the materials were mechanically milled in a 8000M Mixer/Mill® High-Energy Ball Mill for 400 min using stainless steel vial and grinding medium in a ball-to-powder ratio of 20:1. Since the hydrogen storage capacity of the systems is sensibly affected by the amount of Cl^- contained in the additives, the quantity of added $TiCl_3$ was calculated to match the one of the Cl^- contained in $3TiCl_3.AlCl_3$. Therefore, all prepared materials are designated with respect to the amount of Cl^- in the additives as indicated in Table 1. All material handling was carried out in MBraun Unilab glove boxes with oxygen and moisture controlled atmosphere (< 10 ppm of O_2 and H_2O) to prevent oxidation of the samples.

Table 1. Prepared Hydride Mixtures $2LiBH_4 + MgH_2$ and $2LiH + MgB_2$ doped with $TiCl_3$ and $3TiCl_3.AlCl_3$

No.	Materials (The amount of additive is expressed in mol %)	Mol % of added Cl^-	Designation
1	$2LiBH_4 + MgH_2$	-	Li-RHC_a
2	$2LiBH_4 + MgH_2$ + 2.5 mol % $TiCl_3$	7.50	Li-RHC_a+7.5 $TiCl_3$
3	$2LiBH_4 + MgH_2$ + 0.625 mol % ($3TiCl_3.AlCl_3$)	7.50	Li-RHC_a+7.5 ($3TiCl_3.AlCl_3$)

4	$2LiBH_4 + MgH_2$ + 0.9375 mol % ($3TiCl_3.AlCl_3$)	11.2	Li-RHC_a+11.2 ($3TiCl_3.AlCl_3$)
5	$2LiBH_4 + MgH_2$ + 1.25 mol % ($3TiCl_3.AlCl_3$)	15.0	Li-RHC_a+15 ($3TiCl_3.AlCl_3$)
6	$2LiBH_4 + MgH_2$ + 2.5 mol % ($3TiCl_3.AlCl_3$)	30.0	Li-RHC_a+30 ($3TiCl_3.AlCl_3$)
7	$2LiH + MgB_2$ + 2.5 mol % $TiCl_3$	7.50	Li-RHC_d + 7.5 $TiCl_3$
8	$2LiH + MgB_2$ + 0.3125 mol % ($3TiCl_3.AlCl_3$)	3.70	Li-RHC_d+3.7 ($3TiCl_3.AlCl_3$)
9	$2LiH + MgB_2$ + 0.625 mol % ($3TiCl_3.AlCl_3$)	7.50	Li-RHC_d+7.5 ($3TiCl_3.AlCl_3$)
10	$2LiH + MgB_2$ + 2.5 mol % ($3TiCl_3.AlCl_3$)	30.0	Li-RHC_d+30 ($3TiCl_3.AlCl_3$)

2.2. Sample characterization

2.2.1. Volumetric measurements

De-/hydrogenation measurements and hydrogen kinetic behavior of the materials were performed using a custom-built volumetric Sieverts type apparatus. The first dehydrogenation of some samples was measured from room temperature up to 400 °C with a temperature ramp of 3 °C/min under 3 bar of H_2. Hydrogenation-dehydrogenation cycling measurements for all the materials were performed 3 bar hydrogen overpressure at 400 °C for the dehydrogenation and 50 bar at 350 °C for the hydrogenation. The hydrogen kinetic behavior was also evaluated *via* isothermal measurements at 360 °C, 370 °C, 380 °C, 390 °C and 400 °C under 50 bar and 3 bar of hydrogen for hydrogenation and dehydrogenation, respectively. The hydrogenation/dehydrogenation measurements lasted until the plateau was met the criteria: Δwt (%) = 0.0002 and Δt (min) = 1. For hydrogenation and dehydrogenation processes the activation

energies (Ea) were calculated by fitting of the kinetic curves with proper solid-gas models to obtain the kinetic rate constant (k) and by plotting ln(k) vs. 1/T (T = temperature).

2.2.2. Coupled Sieverts with differential scanning calorimetry

Coupled Sieverts-DSC measurements were carried out by using a high-pressure calorimeter (Sensys DSC, Setaram) coupled to a Sieverts-type apparatus (PCTPro-2000, Setaram & Hy-Energy). The high-pressure cell of the calorimeter was loaded with ~ 13-50 mg of the powder sample. The dehydrogenation was performed by heating the sample from room temperature up to 450 °C with a heating rate of 5 °C/min under 3 bar H_2 back pressure and the hydrogenation was carried out with a heating rate of 5 °C/min from room temperature to 350 °C under 50 bar H_2. The calorimetric profiles were evaluated by the Calisto software to obtain the peak temperatures.

2.2.3. Synchrotron powder X-Ray diffraction (SR-PXD)

Ex situ PXD measurements were performed on Bruker D8 Discover in Bragg-Brentano geometry laboratory device equipped with a copper source (λ= 1.54184 Å) and general area detector[35].

In situ SR-PXD was carried out at the beamline I711 at Max-lab II (Lund, Sweden, λ = 0.9938 Å), the measurement time was chosen to be 30 or 60 s for fixed exposure time mode and varied between 50 and 100 s for dose mode. All PXD data was referred to the magnitude of the scattering vector q= 4π sin θ/λ where λ is the X-ray wavelength and 2θ is the scattering angle. The diffracted intensity was measured by a Mar-165 CCD detector. The sample (0.5 mg–2 mg) was airtight encapsulated in a sapphire capillary and then mounted into an in house developed *in situ* cell, which is able to control heating temperatures and operating pressures[36,37]. The 2D diffraction patterns were azimuthally averaged and reduced to 1D diffractograms by using FIT2D program[38].

2.2.4. Magic angle spinning solid-state nuclear magnetic resonance (MAS NMR)

^{11}B MAS NMR spectra of the materials were obtained on a Varian Direct-Drive VNMRS-600 spectrometer (14.1 T) using a custom-built CP/MAS NMR probe for rotors with a diameter of 4 mm. The experiments were performed at room temperature using airtight end-capped zirconia rotors packed with the samples in an argon-filled glovebox (O_2 and H_2O levels were monitored to be below 10 ppm). A spinning speed of υ_R = 12.0 kHz, a 0.5 μs excitation pulse for a ^{11}B rf field strength of $\gamma B1/2\pi \approx 60$ kHz, and a 10 s relaxation delay was employed for each experiment.

2.2.5. High resolution transmission electron microscopy (HR-TEM)

HR-TEM images were obtained on a FEI Titan 80-300 microscope operating at 300 kV. The samples for TEM were prepared by dispersing a small amount of powder on a commercial silicon nitride membrane grid inside a glove box and then directly introducing the specimen into the microscope. The samples were exposed to air for a very short time. TEM image processing was done with the following programs: Digital Micrograph (License n^o. 90294175), i-TEM (License n^o. A2382500) and JEMs (License n^o. IEb59yBDflUMh).

2.2.6. Energy dispersive spectroscopy (EDS)

EDS measurements were performed using a FEI Talos (S)TEM running at 200 kV. The specimen was prepared by suspension of the sample powder in dry cyclohexane and ultrasonicating for 5 min, then one drop was placed on the copper grid and left to dry. Then the sample grid was mounted on the TEM sample holder and inserted for measurement. The data were collected using the ChemiSTEM technology from FEI with an X-FEG electron source and a High Angle Annular Dark Field (HAADF) detector setup.

2.2.7. Small-angle X-ray scattering (ASAXS)

The Ti-ASAXS measurements were performed at the FCM beamline of the PTB installed at the synchrotron radiation facility BESSY II (HZB, Berlin, Germany)[39]. The beamline was combined with the HZB ASAXS instrument[40]. The four-crystal monochromator has an energy resolution of $\Delta E/E \sim 1x10^{-4}$, using the Si (111) crystals[41]. An in vacuum version of a Pilatus 1M detector was used to record the scattering pattern[42]. All measurements were performed at two sample-to-detector distances (0.8 m and 3.70 m) to cover the maximum experimentally accessible q–range. Here, q is the magnitude of the scattering vector: $q = 4\pi \sin\theta/\lambda$, where λ is the wavelength of the radiation and θ is half of the scattering angle. In order to separate the resonant scattering of Ti-containing nanostructures, all measurements were carried out below the K absorption edge of titanium[43]. All selected energies E_i with their corresponding anomalous dispersion factors are listed in ESI Table S1[44]. The samples were mounted on molybdenum sample holder sheets of 0.2 mm thickness with a circular hole of 5 mm in diameter. The samples were supported and sealed within Kapton tape on each side of the sample holder to avoid any change in oxidation state of the samples. They were mounted inside a glovebox. All ASAXS measurements were integrated and corrected for detector responsivity and sample transmission. For each measurement a sample of Ag-behenate powder was measured as a standard for the q-axis in order to merge the curves measured at two different distances. Additionally, a glassy carbon standard was measured for all samples to convert the measured intensities to an absolute scale. The anomalous scattering contribution caused by the Ti containing structures was separated by using the method described in Haas *et al.*[45]. The curves for the scattered intensity $I(q,E_i)$ were fitted simultaneously for all energies, assuming spherical particles, according to:

$$I(q, E_i) = \Delta\rho^2(E_i) \int N(r)\Psi^2(r, q)dr + Kq^{-x} + B(E_i) \quad (1)$$

where $\Delta\rho(E_i)$ is the electron density difference between particles and matrix, $N(r)$ the particle size distribution, r the particle radius and $\psi(r,q)$ the form factor for spherical particles. The term

Kq^{-x} summarizes scattering contributions from larger constituents, while $B(E_i)$ describes the energy-dependent background (fluorescence and resonant-Raman scattering) and the scattering originating from surface roughness and large scale correlations of the powder. The form factor for spheres was given by:

$$\Psi(r,q) = \frac{4}{3}\pi r^3 \frac{sin(qr) - qrcos(qr)}{(qr)^3} \qquad (2)$$

To account for the polydispersity of Ti-containing particles in the hydride matrix, a normalized log-normal distribution was assumed:

$$N(r) = \frac{1}{\sqrt{2\pi\sigma\, r}} exp\left[-\frac{ln(r/R)^2}{2\sigma^2}\right] \qquad (3)$$

with σ being the standard deviation of the distribution and R the mean radius. For the fitting procedure of the volume-weighted size distribution, the program SASfit has been used[46].

2.3. Thermodynamic calculations

To determine the nature of the Al and Ti containing species, thermodynamic calculations were carried out using the HSC Chemistry software[47]. The calculations were done based on the reactivity of the Li-RHC_d/Li-RHC_a with $3TiCl_3.AlCl_3$, respectively, under different temperature and pressure conditions. The most favorable reactions were identified through a combination of Gibbs minimization equilibrium with selected solid and gas species. The obtained results represent ideal phase equilibrium compositions useful to predict possible reaction mechanisms between the Li-RHC_d/Li-RHC_a matrix and the additive involving solid products and gaseous species such as B_2H_6, B_xH_y (x= 5 to 12, y = 5 to 14) and $B_xH_yCl_z$ (x= 1, y = 1 and 2, z = 1 and 2). For all the calculations the solid orthorhombic $LiBH_4$ (Pnma) was taken into account. Al-Ti alloys as well as MB_2 (M = Ti and Al) were considered as possible products. $Li_2B_{12}H_{12}$ was not taken into account owing to the lack of available physicochemical data.

3. RESULTS

3.1. Volumetric and calorimetric investigations

The influence of the amounts of the additive on the first non-isothermal dehydrogenation behavior as well as on the kinetic rates of the undoped and doped Li-RHC_a mixtures have been investigated in a volumetric Sieverts apparatus (Fig. 1). In Fig. 1A the effect of two different additives ($TiCl_3$ and $3TiCl_3.AlCl_3$) in the Li-RHC_a system are compared. The dehydrogenation reactions of all samples occur in two consecutive steps. The first step corresponds to the dehydrogenation of MgH_2 to Mg and releases approximately 2.8 wt.% of hydrogen. In the second step, the reaction between Mg and $LiBH_4$ to form MgB_2 and LiH takes place with the release of about 8.5 wt.% of H_2[17]. In the case of the undoped Li-RHC_a (Fig. 1A(a), B(a)), a long incubation period of about 10 hours is observed between the two dehydrogenation steps. This long interval between the two reaction steps is considerably reduced for the case of Li-RHC_a+7.5$TiCl_3$ and Li-RHC_a+7.5($3TiCl_3.AlCl_3$), as can be seen in Fig. 1A(b) and (c). From the literature, it is well known that the addition of $TiCl_3$ to Li-RHC notably enhances its kinetic behavior[16,31,48]. However, for future use of such a material in mobile applications, $TiCl_3$ cost (~ 80 USD/g) is a major constraint for the design of a solid-state hydrogen storage reservoir[49]. For these reasons, a Ti based cost efficient additive composed of $3TiCl_3.AlCl_3$ (~ 0.50 USD/g) is here utilized[50]. Fig. 1B shows clearly that the increase in the molar amount of the cost effective $3TiCl_3.AlCl_3$ additive from 7.5 to 30 mol % of added Cl^- avoids the described incubation period. However, as a consequence of the increased amount of the $3TiCl_3.AlCl_3$ additive, the hydrogen capacity considerably decreases from about 10 wt.% to 8 wt.% H_2.

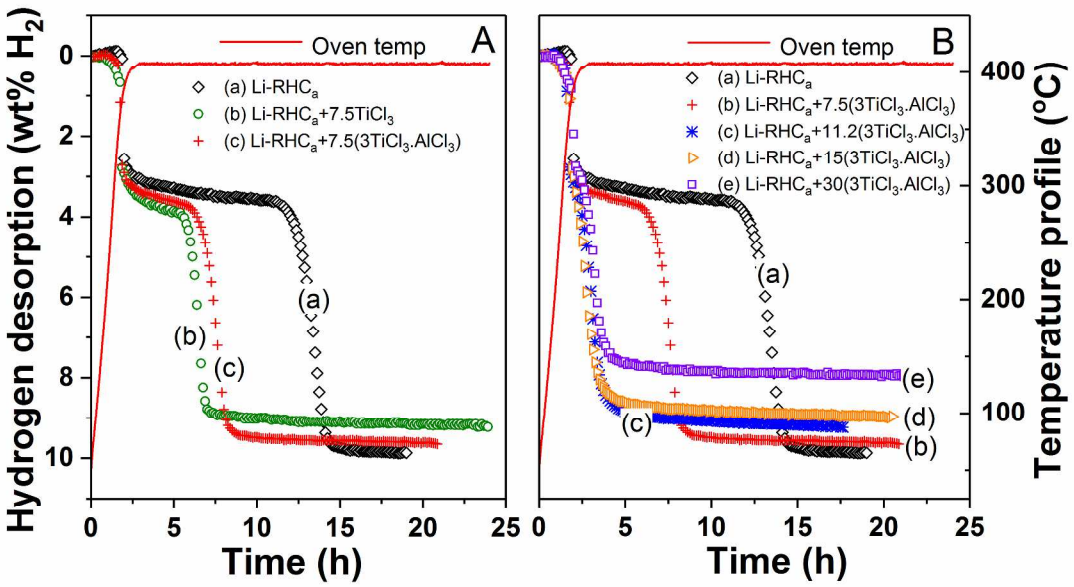

Figure 1. First dehydrogenation reaction of the Li-RHC_a composite systems measured from RT to 400°C, heating rate 3 °C/min, under P_{H2}= 3 bar. **A** (a) undoped Li-RHC_a; (b) Li-RHC_a+7.5$TiCl_3$, (c) Li-RHC_a+7.5(3$TiCl_3$.$AlCl_3$). **B** (a) undoped Li-RHC_a, (b) Li-RHC_a+7.5(3$TiCl_3$.$AlCl_3$), (c) Li-RHC_a+11.2(3$TiCl_3$.$AlCl_3$), (d) Li-RHC_a+15(3$TiCl_3$.$AlCl_3$), (e) Li-RHC_a+30(3$TiCl_3$.$AlCl_3$).

Several samples composed of Li-RHC_a and Li-RHC_d plus different contents of 3$TiCl_3$.$AlCl_3$ and $TiCl_3$ additives have been cycled 20 times (ESI Fig. S1). Fig. 2 summarizes the evolution of the hydrogen capacity for the tested compositions. The addition of both additives ($TiCl_3$ and 3$TiCl_3$.$AlCl_3$) has a clear beneficial effect on the hydrogen storage capacity of the Li-RHC_d (Fig. 2B) rather than on Li-RHC_a (Fig. 2A, ESI Table S2). The Li-RHC_d+7.5(3$TiCl_3$.$AlCl_3$) material possesses the highest hydrogen capacity, i.e. around 9.5 wt.% H_2, and a stable cycling behavior, i.e. the loss of capacity is smaller than 1 wt.%. The reduced capacity over the cycling period for most of the Li-RHC_a compositions is above 1 wt.% (Fig. 2A(a)-(c), ESI Table S2), except for the system with large amount of additive (Fig. 2A(d), ESI Table S2). In contrast, when starting from

the desorbed state (Li-RHC$_d$) with 7.5TiCl$_3$, 7.5 and 30(3TiCl$_3$.AlCl$_3$) exhibit a drop of capacity below 1 wt.% (Fig. 2B(a), (c), (d), ESI Table S2). The Li-RHC$_d$+3.7(3TiCl$_3$.AlCl$_3$), instead, shows the largest decrease of capacity (> 2 wt.%) upon cycling (Fig. 2B(b), ESI Table S2). Fig. 2A and 2B also show that hydrogen capacity is not always in correlation with the amount of additive, i.e. some compositions with lower amount of additive exhibit decreased hydrogen capacities (Fig. 2A(b) and Fig 2B(b)). In addition, the material Li-RHC$_d$+3.7(3TiCl$_3$.AlCl$_3$) exhibits a fast deterioration of the reversible hydrogen capacity. These facts can be attributed to the non-homogenous distribution of the additive all over the base material (Li-RHC).

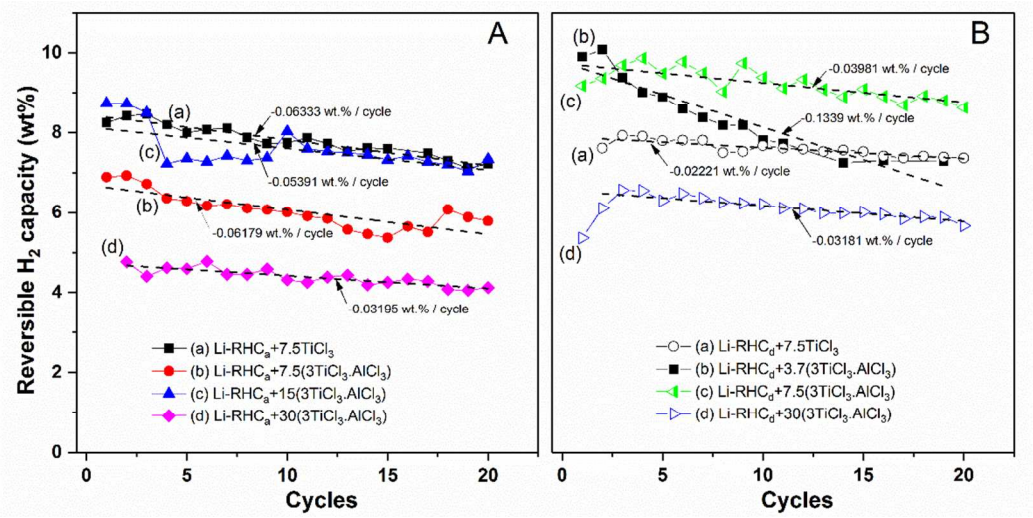

Figure 2. Reversible hydrogen storage capacities versus number of cycles based on the desorption curves. Cycling process preformed at 350 °C and 400 °C under 50 bar and 3 bar of H_2 for the hydrogenation and dehydrogenation, respectively. **A** sample prepared in the hydrogenated state (Li-RHC$_a$). **B** sample prepared in the dehydrogenated state (Li-RHC$_d$).

Fig. 3 shows the time required to reach 95% of the total hydrogen storage capacity during hydrogenation and dehydrogenation. In the case of the TiCl$_3$ additive, Li-RHC$_a$+7.5TiCl$_3$ presents better hydrogenation-dehydrogenation kinetic performance than Li-RHC$_d$+7.5TiCl$_3$ (ESI Table S2). As seen in Fig. 3A(a) and B(a), the material Li-RHC$_a$+7.5(3TiCl$_3$.AlCl$_3$) exhibits

the slowest kinetic performance. However, the Li-RHC_d+7.5($3TiCl_3.AlCl_3$) material possesses the shortest hydrogenation-dehydrogenation times (~ 30 min). A further increment of the amount of $3TiCl_3.AlCl_3$ does not lead to faster kinetic behavior.

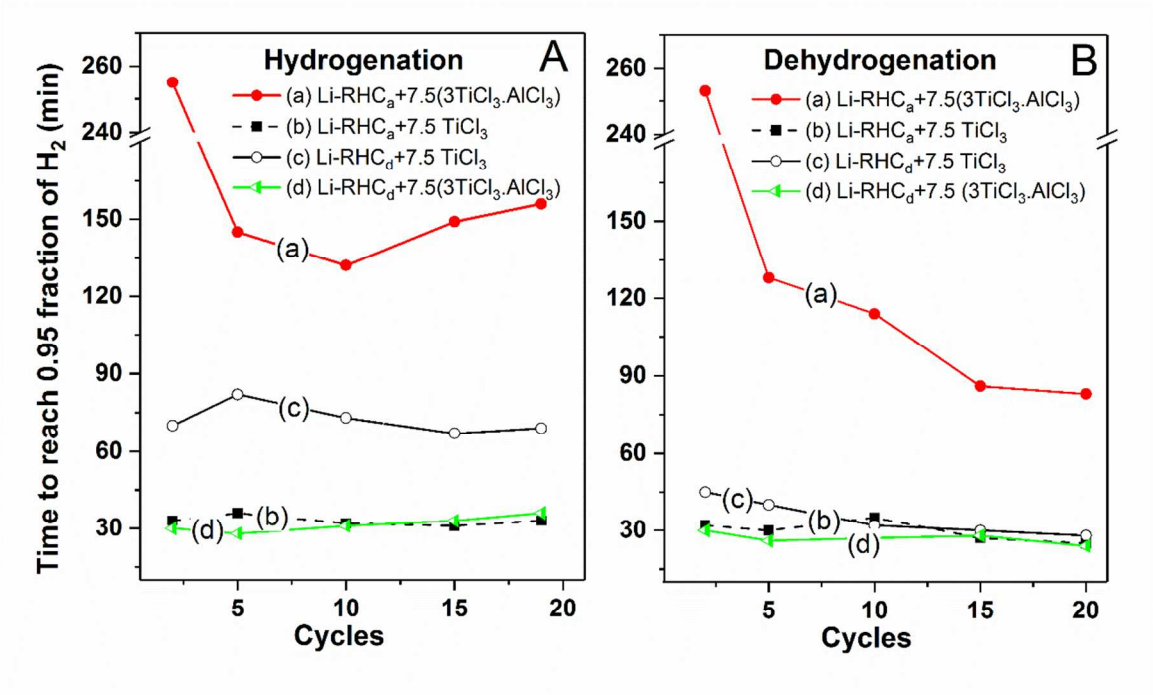

Figure 3. Time to reach 95% of the maximum hydrogen content versus the number of cycles: **A** hydrogenation from the 2nd to the 19th cycle and **B** dehydrogenation from 2nd to 20th cycle. The cycling process is performed at 350 °C and 400 °C, under 50 bar and 3 bar of H_2 for the hydrogenation and dehydrogenation, respectively. The hydrogen fraction was determined from the normalization of the kinetic curves taking as a reference the actual hydrogen capacity.

Calorimetric measurements coupled with Sieverts apparatus for Li-RHC_d, Li-RHC_d+7.5$TiCl_3$ and Li-RHC_d+7.5($3TiCl_3.AlCl_3$) (ESI Fig. S2) show endothermic events related to the $LiBH_4$ phase transition (event I), $LiBH_4$ melting (event II) and hydrogen release (events III and IV)[51,52]. Events (I and II) are slightly shifted toward lower temperatures in the doped materials. Events III and IV are associated to the dehydrogenation reaction of MgH_2 and $LiBH_4$ e with simultaneous

formation of MgB_2, respectively[17,52]. These endothermic events related to the hydrogen release are in agreement with the coupled Sieverts measurements in the range of temperatures between 330 °C and 450 °C. The dehydrogenation temperature of MgH_2 is roughly 20 °C lower in the doped hydrogenated materials Li-RHC_d+7.5($3TiCl_3.AlCl_3$) and Li-RHC_d+7.5$TiCl_3$ (ESI Fig. S2(b) and (c)) in comparison to the undoped hydrogenated Li-RHC_d (ESI Fig. S2(a)). The onset temperature for the decomposition of $LiBH_4$ in the doped materials is at about 390 °C whereas that for the undoped material is at around 440 °C. From the volumetric curves, it is clear that the dehydrogenation processes for the doped materials are almost completed (ESI Fig. S2(e) and (f)) when reaching the final temperature of 450 °C. However, for the undoped material the second step of the dehydrogenation barely starts at 450 °C with a release of hydrogen of just 3.0 wt.% (ESI Fig. S2(d)).

3.2. Characterization of the crystalline and non-crystalline phases: *ex situ*, *in situ* PXD and ^{11}B MAS-NMR measurements

The Li-RHC_d+7.5($3TiCl_3.AlCl_3$) material has the best performance in terms of hydrogen storage capacity, kinetic behavior and stability upon cycling (Fig. 2 and 3, ESI Table S2). In addition, it presents enhanced thermal properties in comparison with the undoped material (ESI Fig. S2). Hence, the material containing 7.5($3TiCl_3.AlCl_3$) has been characterized and compared with the doped $TiCl_3$ material with the same amount of Cl^- (7.5$TiCl_3$). Fig. 4 shows the *ex situ* PXD (A) diffraction patterns and ^{11}B MAS NMR spectra (B) of the Li-RHC_d+7.5($3TiCl_3.AlCl_3$) and Li-RHC_d+7.5$TiCl_3$ after milling and cycling. The patterns of the Li-RHC_d+7.5($3TiCl_3.AlCl_3$) and Li-RHC_d+7.5$TiCl_3$ after milling (Fig. 4A(a), 4A(c)) exhibit reflections of MgB_2, LiH and LiCl. After 20 cycles, the samples in dehydrogenated states (Fig. 4A(b) and (d)) show the presence of the phases found after milling and free Mg (always present in the as received MgB_2).

In situ PXD measurement during heating, hydrogenation, dehydrogenation and cooling for the Li-RHC_d+7.5($3TiCl_3.AlCl_3$) sample after previous 20 cycles has been performed (ESI Fig. S3). At room temperature and during heating up to 350 °C, MgB_2, LiH, LiCl and elemental Mg are found. Upon hydrogenation at 350 °C under 50 bar H_2, the disappearance of residual Mg and MgB_2 are followed by the formation of MgH_2. At these temperatures, $LiBH_4$ is not observed because it is in its molten state. At the end of the isothermal period at 50 bar H_2 pressure, the reflections of unreacted MgB_2 are still visible. However, the LiCl peaks are not visible anymore. After decreasing the pressure to 5 bar H_2 and increasing the temperature up to 400 °C, Mg and then MgB_2 reflections appear[17,24]. During the cooling period, the reappearance of the LiCl at 275 °C is noticed. In the case of the material prepared in hydrogenated state (i.e. Li-RHC_a+7.5($3TiCl_3.AlCl_3$) and Li-RHC_a+7.5$TiCl_3$), both the *ex situ* and *in situ* PXD (ESI Fig. S4 and S5) show similar behavior as the material prepared starting from the dehydrogenated state (Li-RHC_d). The *ex situ* PXD of the material after milling (ESI Fig. S4) exhibits the presence of $LiBH_4$, MgH_2 and LiCl, while after 20 cycles the material in desorbed state shows the presence MgB_2, LiH, LiCl and free Mg. Moreover, the *in situ* PXD for the dehydrogenation mechanism starting from as-milled Li-RHC_a+7.5($3TiCl_3.AlCl_3$) is similar to the one described above for the Li-RHC_d+7.5($3TiCl_3.AlCl_3$) after 20 cycles (ESI Fig. S5). Interestingly, the presence of the additives, i.e. $TiCl_3$, $3TiCl_3.AlCl_3$, and crystalline Ti and Al containing phases, are not detected by PXD (Fig. 4A, ESI Fig. S3-S5).

^{11}B MAS NMR spectra of the milled and the cycled Li-RHC_d+7.5($3TiCl_3.AlCl_3$) and Li-RHC_d+7.5$TiCl_3$ materials are shown in Fig. 4B. The spectra of the ball milled samples (Fig. 4B (a) and 4B (c)) are nearly identical and are dominated by the central-transition resonances from MgB_2 with the centerband resonance at 100.3 ppm. In addition, the analysis of central transition

intensities of the spectra show a low-intensity centerband resonance is observed at 5.2 ppm, which constitutes 8.4 % and 5.1 % of the total ^{11}B NMR intensity for the as-milled Li-RHC$_d$+7.5(3TiCl$_3$.AlCl$_3$) and Li-RHC$_d$+7.5TiCl$_3$ materials, respectively.

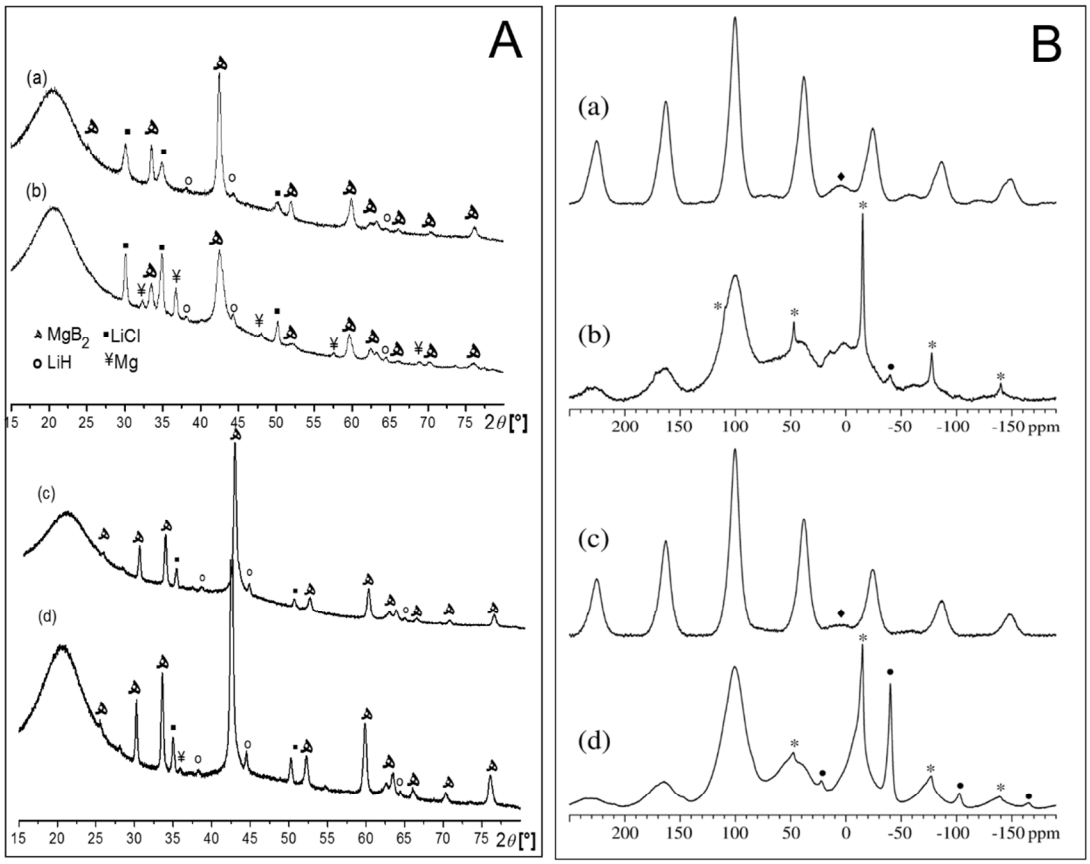

Figure 4. **A** *Ex situ* PXD and **B** ^{11}B MAS NMR spectra (14.1 T, υR = 12.0 kHz) of the doped samples prepared in the dehydrogenated state: (a) Li-RHC$_d$+7.5(3TiCl$_3$.AlCl$_3$) after milling, (b) Li-RHC$_d$+7.5(3TiCl$_3$.AlCl$_3$) after the 20th cycle, (c) Li-RHC$_d$+7.5TiCl$_3$ after milling and (d) Li-RHCd+7.5TiCl3 after the 20th cycle. The diamonds (♦) indicate the 5.2 ppm centerband, observed for the two ball-milled samples, whereas centerband and spinning sideband resonances from $Li_2B_{12}H_{12}$ and $LiBH_4$ are indicated by asterisks (∗) and solid circles (•), respectively.

The ^{11}B NMR spectra of the cycled materials (Fig. 4B (b) and 4B (d)) are more complicated because of overlapping resonances (centerbands and spinning sidebands) of the boron-containing phases. In addition to MgB_2, which is still the dominate phase in both cycled materials, resonances from unreacted $Li_2B_{12}H_{12}$ at -15.2 ppm and $LiBH_4$ at -40.5 ppm are also observed. For the Li-RHC_d+7.5($3TiCl_3.AlCl_3$) material (Fig. 4B (b)), two additional centerbands appear at 2.4 ppm and 15.9 ppm, which could not be assigned to any specific phase and are thus, denoted unknown phases, UP(1) and UP(2), respectively. The 2.4 ppm peak might potentially originate from AlB_2, following an earlier ^{11}B NMR spectrum obtained for this phase at identical conditions. A deconvolution of the central transition region for the cycled Li-RHC_d+7.5($3TiCl_3.AlCl_3$) material, including centerbands and spinning sidebands, gives the following relative ^{11}B NMR intensities for the individual phases: 63.0 % MgB_2, 12.2 % $Li_2B_{12}H_{12}$, 0.6 % $LiBH_4$, 20.9 % UP(1) and 3.3 % UP(2). The UP(1) and UP(2) resonances are not identified for the cycled Li-RHC_d+7.5$TiCl_3$ material (Fig. 4B (d)), which on the contrary includes a new resonance at approx. -6.3 ppm (UP(3)). This resonance is clearly visible as a high-frequency shoulder to the narrow centerband resonance from $Li_2B_{12}H_{12}$ at -15.2 ppm, which gives a strong contribution to the spinning sidebands at 50 ppm, -30 ppm, and -135 ppm. A simulation of this spectrum results in the relative intensities: 59.2 % MgB_2, 7.1 % $Li_2B_{12}H_{12}$, 6.5 % $LiBH_4$, and 27.3 % UP(3). A resonance from TiB_2 at -4.9 ppm is expected for all cycled samples. However, this signal is not observed in the NMR spectra.

3.3. Nanostructure and distribution of the Ti-rich phase: ASAXS measurement

The volume weighted size distributions of the Ti rich nanosized particles obtained by ASAXS measurements for the as-milled and cycled Li-RCH_d plus $TiCl_3$ and ($3TiCl_3.AlCl_3$) samples are

shown in Fig. 5. Li-RHC_d+7.5$TiCl_3$ in the as-milled state has been measured as a reference sample and the resulting ASAXS curves are shown in ESI Fig. S6, exemplarily. At *q*-values around 1 nm^{-1} the curves show a clear resonant scattering structure. At very high *q*-values above about 2.5 nm^{-1}, incoherent and inelastic scattering contributions limit the further decrease of the scattered intensity. In the lower *q*-region the curves become off-resonant and follow a power law behavior. The exponent of the power-law amounts to 3.6, implying mass fractals with dense bulk and rough surfaces. Fig. 5 shows that the as-milled Li-RHC_d+7.5$TiCl_3$ and Li-RHC_d+7.5(3$TiCl_3$.$AlCl_3$) mainly differ in their polydispersity. The normalized standard deviation of the size distribution for as-milled Li-RHC_d+7.5$TiCl_3$ is 0.38 whereas the corresponding value for the as-milled Li-RHC_d+7.5(3$TiCl_3$.$AlCl_3$) amounts to 0.57, which is around 33 % larger. The mean radius for as-milled Li-RHC_d+7.5$TiCl_3$ is around 3.6 nm while this value is about 32 % (5.3 nm) larger for the as-milled Li-RHC_d+7.5(3$TiCl_3$.$AlCl_3$). For the Li-RHC_d+7.5(3$TiCl_3$.$AlCl_3$) material after 20th cycles, the mean nanoparticle radius after 20 cycles decreases to about 3.5 nm. Increasing the amount of the 3$TiCl_3$.$AlCl_3$ additive does not change significantly the size distribution as seen for Li-RHC_d+30(3$TiCl_3$.$AlCl_3$).

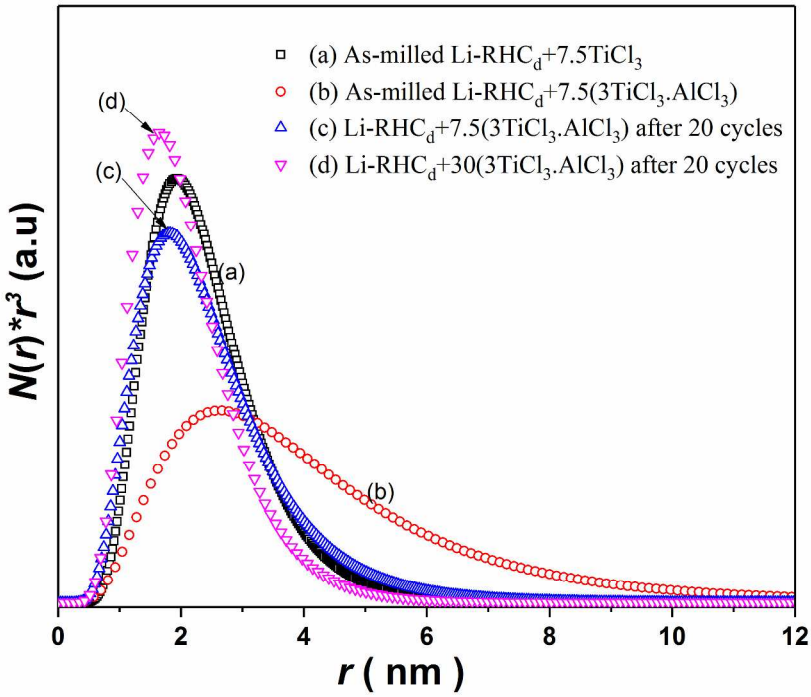

Figure 5. Volume weighted size distributions of Ti rich - nanosized particles obtained by ASAXS for (a) as-milled Li-RHC$_d$+7.5TiCl$_3$, (b) as-milled Li-RHC$_d$+7.5(3TiCl$_3$.AlCl$_3$), (c) Li-RHC$_d$+7.5(3TiCl$_3$.AlCl$_3$) after 20 cycles, (d) Li-RHC$_d$+30(3TiCl$_3$.AlCl$_3$) after 20 cycles.

4. DISCUSSION

Hydrogen storage properties of Li-RHC have been notably improved by the addition of 3TiCl$_3$.AlCl$_3$ (section 3.1). It has been shown that the Li-RHC$_d$+7.5(3TiCl$_3$.AlCl$_3$) material exhibits the best performance upon cycling with a stable capacity of about 9.5 wt. % H_2 and reduced hydrogenation and dehydrogenation times of about 30 min. The characterization of the crystalline and non-crystalline phases in the Li-RHC$_d$+7.5(3TiCl$_3$.AlCl$_3$) after milling and cycling has been performed via *ex situ* and *in situ* PXD (Fig. 4A, ESI Fig. S3-S5) and ^{11}B MAS NMR (Fig. 4B), respectively. ASAXS results (Fig. 5) show that Ti rich nanosized particles are dispersed in the sample. Therefore, to shed light on the nature of the additive within the hydride system and to understand the reasons laying behind the observed beneficial effect on the

material's hydrogenation/dehydrogenation properties, the collected results are herein discussed in detail.

4.1. Phase equilibrium compositions: Thermodynamic calculations

In order to infer the crystalline and amorphous phases obtained by the interaction of Li-RHC and $3TiCl_3.AlCl_3$, phase composition equilibrium calculations based on the Gibbs free energy minimization have been carried out with the HSC Chemistry software[47]. Taking into account the experimental results obtained from the characterizations of the materials (Fig. 4A and B, ESI Fig. S3-S5), the calculations for Li-RHC_d+7.5($3TiCl_3.AlCl_3$) and Li-RHC_a+7.5($3TiCl_3.AlCl_3$) materials under different conditions such as mechanical milling (MM), first hydrogenation and first dehydrogenation have been performed. In several works[25-34], it has been proposed the formation of transition metal borides from the interaction between the Li-RHC material and transition metal based compounds. For the Li-RHC doped with $3TiCl_3.AlCl_3$ (ESI Table S3), the calculations show that the formation of TiB_2 and AlB_2 upon milling is thermodynamically feasible for both the dehydrogenated (Li-RHC_d) and hydrogenated (Li-RHC_a) states as shown in reaction (4) and (5), respectively. These boride species remain stable upon cycling (ESI Table S3).

(4) $0.072LiH_{(s)} + 0.024MgB_{2(s)} + 0.06(3TiCl_3.AlCl_3)_{(s)} \rightarrow 0.072LiCl_{(s)} + 0.024Mg_{(s)} + 0.006AlB_{2(s)} + 0.018TiB_{2(s)} + 0.036H_{2(g)}$

$\Delta G_{1bar,\ 25\ °C} = -10.9$ kJ

(5) $0.072LiBH_{4(s)} + 0.006(3TiCl_3.AlCl_3)_{(s)} \rightarrow 0.018TiB_{2(s)} + 0.072LiCl_{(s)} + 0.006AlB_{2(s)} + 0.024B_{(s)} + 0.144H_{2(g)}$

$\Delta G_{1bar,\ 25\ °C} = -4.4$ kJ

Instead, if we consider the possible formation of Al-Ti alloys (ESI Table S4), the phase composition equilibrium calculations hint at the formation of the $AlTi_3$ alloy during milling as

described in reactions (6) and (7) for the Li-RHC_d and Li-RHC_a, respectively. The calculations also suggest that this $AlTi_3$ alloy remains stable upon cycle once formed (ESI Table S3).

(6) $0.072LiH_{(s)} + 0.06(3TiCl_3.AlCl_3)_{(s)} \rightarrow 0.072LiCl_{(s)} + 0.006AlTi_{3(s)} + 0.036H_{2(g)}$

$\Delta G_{1bar,\ 25\ ^\circ C} = -7.6$ kJ

(7) $0.072LiBH_{4(s)} + 0.006(3TiCl_3.AlCl_3)_{(s)} \rightarrow 0.072LiCl_{(s)} + 0.006AlTi_{3(s)} + 0.072B_{(s)} + 0.144H_{2(g)}$

$\Delta G_{1bar,\ 25\ ^\circ C} = -3.5$ kJ

The formation of titanium boride species (TiB_2 and AlB_2) is thermodynamically more favorable than the formation of the $AlTi_3$ alloy. Nonetheless, the characterization of the materials evidences certain discrepancy with the formation of the transition metal boride species (Fig. 4, ESI Fig. S3-S5). In the case of Li-RHC_d+7.5($3TiCl_3.AlCl_3$) and Li-RHC_a+7.5($3TiCl_3.AlCl_3$), the diffraction patterns after milling do not show the presence of free Mg as proposed in reaction (4), unless this phase is not detected due to its low amount (Fig. 4A(a) and Fig. S4 A(a)). Additionally, the NMR spectrum of the Li-RHC_d+7.5($3TiCl_3.AlCl_3$) material after cycling does not evidence clearly the presence of any transition metal boride species (Fig. 4 B (b)). On the contrary, the formation of the $AlTi_3$ alloy after milling and after cycling appears to be likely (Fig. 4A(a), (b) and 4B(a) and (b)) since neither the presence of free Mg nor the formation of transition metal boride species are included in reactions (6) and (7). Therefore, the formation of TiB_2 and AlB_2 might be kinetically restricted, so that the formation of the $AlTi_3$ alloy takes place.

4.2. Nature of the nanosized additive: HR-TEM

Experimental results indicate that the additive ($3TiCl_3.AlCl_3$) interacts with Li-RHC (Fig. 4) and provides the *in situ* formation of nanostructured Ti-rich phase distributed on the MgB_2 particles (ESI Fig. S7). The phase equilibrium thermodynamic calculations suggest that the

nanosized Ti-rich phase is composed of Al and Ti, specifically $AlTi_3$ alloy. Therefore, to verify the nature of the nanosized Ti-rich phase, HR-TEM observations combined with the analysis of the fast Fourier transformation analysis (FFT) and simulations of the electron diffraction pattern (DP) in Zone Axis (ZA) condition have been performed on several particles. Fig. 6 shows the HR-TEM micrographs and their respective analysis (FFT and simulated DP). The presence of nanosized particles of hexagonal $AlTi_3$ and cubic $AlTi_2$ is observed in the material after milling (Fig. 6A) . Upon cycling (Fig. 6B and C), hexagonal $AlTi_3$ and cubic $AlTi_2$ are still seen and the appearance of cubic $AlTi_3$ is noticed. The same Al-Ti alloys as for the Li-RHC_a+7.5($3TiCl_3.AlCl_3$) are also observed (ESI Fig. S8). It is important to point out that the most frequently identified nanoparticles belong to the hexagonal $AlTi_3$ phase. Mroevoer, Mg-Al alloys, Mg-Al-B compounds as well as TiB_2 and AlB_2 have not been identified *via* HR-TEM.

These HR-TEM observations confirm the formation of nanosized AlTi alloys, mainly the hexagonal $AlTi_3$, as predicted with the equilibrium thermodynamic calculations as shown in reaction (6) and (7), and in ESI Table S3 and S4. This is in concordance with the PXD analysis (Fig. 4A(a) and (b)) since no Al-Ti crystalline phase has been detected. NMR spectra (Fig. 4B) show the presence of a peak that might belongs to AlB_2 (UP1) and of another peak which cannot be attributed to any boron containing species (UP2). Considering the HR-TEM observation, it is possible to discard AlB_2 as a potentially or at least dominantly formed phase. Regarding the size of the Al-Ti alloys nanoparticles, it is possible to see in Fig. 6 that the sizes of the hexagonal $AlTi_3$ after milling and cycling are in the range of 1 to 10 nm and 1 to 5 nm, respectively. These findings are in good agreement with the ASAXS results (Fig. 5).

4.3. Effect of the $3TiCl_3.AlCl_3$ additive on Li-RHC

4.3.1. Interfacial energy minimization: d–value mismatch

In the previous section, the *in situ* formation of AlTi alloys (Section 4.2) has been verified by HR-TEM observation. It has been reported that phases with similar crystal structure as MgB_2 can act as heterogeneous nucleation sites for its formation[25]. Several transition metal borides such as TiB_2, NbB_2 and VB_2 are able to provide coherent interfaces to enhance the heterogeneous nucleation and growth of hexagonal MgB_2[25-32,53]. There are three necessary requirements for an effective heterogeneous nucleation: the most important is a low interfacial energy between the nucleation agent and the nucleate new phase (MgB_2), the second is sufficiently high amount of the nucleation agent and the third is the homogenous distribution of the nucleation agent[25,54,55]. A sufficient condition for interfacial energy minimization is a minimized lattice mismatch in consecutive atom rows across an interface. To achieve the minimized lattice mismatch condition, the inter-planar spaces (d–value) between the closed-packed planes of the nucleation agent and the MgB_2 should be lower than the critical d–value mismatch of 6 % [54]. In our case, no transition-metal boride species have been detected as a product of the interaction between Li-RHC material and the $3TiCl_3.AlCl_3$ additive (Fig. 4 and Fig. 6). For this reason and considering that the AlTi alloys can potentially act as an effective heterogeneous nucleation center for MgB_2, their d–value mismatches have been calculated. These parameters have been determined from the diffraction cards of the AlTi alloys determined via HR-TEM (Fig. 6): hexagonal-$AlTi_3$ (ICSD 191189), cubic-$AlTi_3$ (ICSD 189695) and cubic-$AlTi_2$ (ICSD 189696). The d–value mismatch for the closed-packed planes between the AlTi alloys and MgB_2 are: $MgB_2\{1011\}$//hexagonal-$AlTi_3\{2021\}$ =3.3 %; $MgB_2\{1010\}$//cubic-$TiAl_3\{2020\}$= 31.9 % and $MgB_2\{1010\}$//cubic-$TiAl_2\{2020\}$= 35.0 %. As seen, the hexagonal $AlTi_3$ phase, the most frequent identified phase, shows a suitable d–value mismatch well below 6 %. Thus, it fulfils the first above-mentioned requirement for an efficient heterogeneous nucleation of MgB_2. Moreover, based on the observed

kinetic improvement of the Li-RHC_d+7.5($3TiCl_3$.$AlCl_3$) (Fig. 3) and according to the ASAXS (Fig. 5), EDS in STEM-HAAFD mode (ESI Fig. S7) and HR-TEM results (Fig. 6), the *in situ* formed nanosized hexagonal-$AlTi_3$ phase covers the second and third requirement since the proper amount of its nanoparticles is well distributed and upon cycling is located on the formed MgB_2 to assure an enhanced heterogeneous nucleation of new MgB_2 seeds.

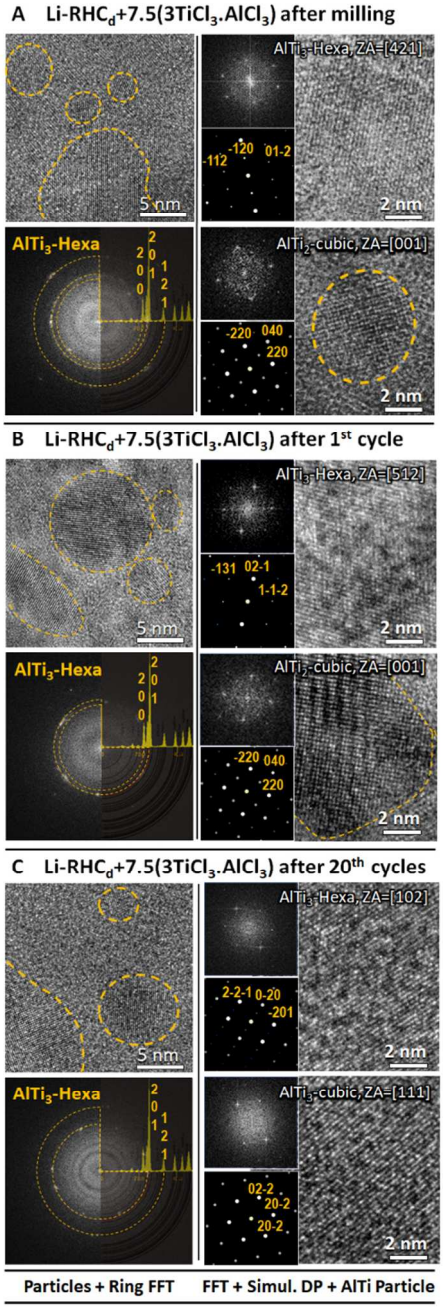

Figure 6. HR-TEM characterization of the nanosized AlTi alloys in Li-RHC_d+7.5($3TiCl_3.AlCl_3$) material **A** after milling, **B** after 1st cycle (sample in dehydrogenated state) and **C** after 20th cycle (sample in dehydrogenated state). FFT was calculated in each region and compared to simulated diffraction patterns (DPs) in the adequate orientation; the width of the FFT and corresponding simulations is 18 nm^{-1}. Structure cards: hexagonal $AlTi_3$ ICSD 191189, cubic $AlTi_3$ ICSD 189695, cubic $AlTi_2$ ICSD 189696.

4.3.2. First dehydrogenation of Li-RHC_a: effects on the incubation period

It has been already reported that the reaction pathways of Li-RHC depend on the temperature and hydrogen pressure conditions[24]. $LiBH_4$ and MgH_2 individually decompose and do not form MgB_2 under 1 bar of H_2 overpressure in the temperature range from 400 to 450 °C, hindering the reversibility of Li-RHC[14,24]. The dehydrogenation of Li-RHC proceeds in three steps when it is carried out in the pressure range from 3 to 5 bar of H_2: (1) fast decomposition of MgH_2, (2) incubation period with a small hydrogen release and (3) reaction between free Mg and $LiBH_4$ to form MgB_2 and LiH. The incubation period is attributed to the reaction (8), which leads to the individual reaction of $LiBH_4$ into $Li_2B_{12}H_{12}$ and not to the $LiBH_4$ decomposition to LiH, B and H_2 (reaction (9)) because of the thermodynamic stability of the reactions, i.e. 56 kJ/mol H_2 and 75 kJ/mol H_2, respectively[14,56-58]:

(8) $2LiBH_{4(l)} \rightarrow (1/6)Li_2B_{12}H_{12(s)} + (5/3)LiH_{(s)} + (13/6)H_{2(g)}$

(9) $LiBH_{4(l)} \rightarrow LiH_{(s)} + B_{(s)} + (3/2)H_{2(g)}$

As proposed in the literature about $LiBH_4 + YH_3$[59,60] and $2LiBH_4 + MgH_2$[57], reaction (8) may not proceed by the intermediate formation of gaseous di-borane (B_2H_6)[61,62] since the gas overpressure kinetically suppresses its formation. It has been proposed that the sluggish kinetic behavior of the first dehydrogenation of Li-RHC is associated with the formation of $Li_2B_{12}H_{12}$

(reaction (8)) as an intermediate phase which blocks the direct contact between $LiBH_4$ and Mg[14]. It has been found that at 450 °C under 10 bar of H_2 overpressure, the formation of $Li_2B_{12}H_{12}$ is avoided because the equilibrium pressure of reaction (8) is below 10 bar (~ 9 bar[10]), enhancing the dehydrogenation kinetic behavior compared to that at lower overpressure conditions[57]. ^{11}B MAS NMR spectra of as-purchased $LiBH_4$, pristine Li-RHC_a and Li-RHC_a+15($3TiCl_3.AlCl_3$) materials after milling and partially dehydrogenated are shown in Fig. 7. The pressure conditions selected for the partially dehydrogenated samples are the reported equilibrium pressures for the reaction between Mg and $LiBH_4$ to form MgB_2 and LiH (3 bar H_2 at 350 °C and 8 bar H_2 at 400 °C)[63,64].

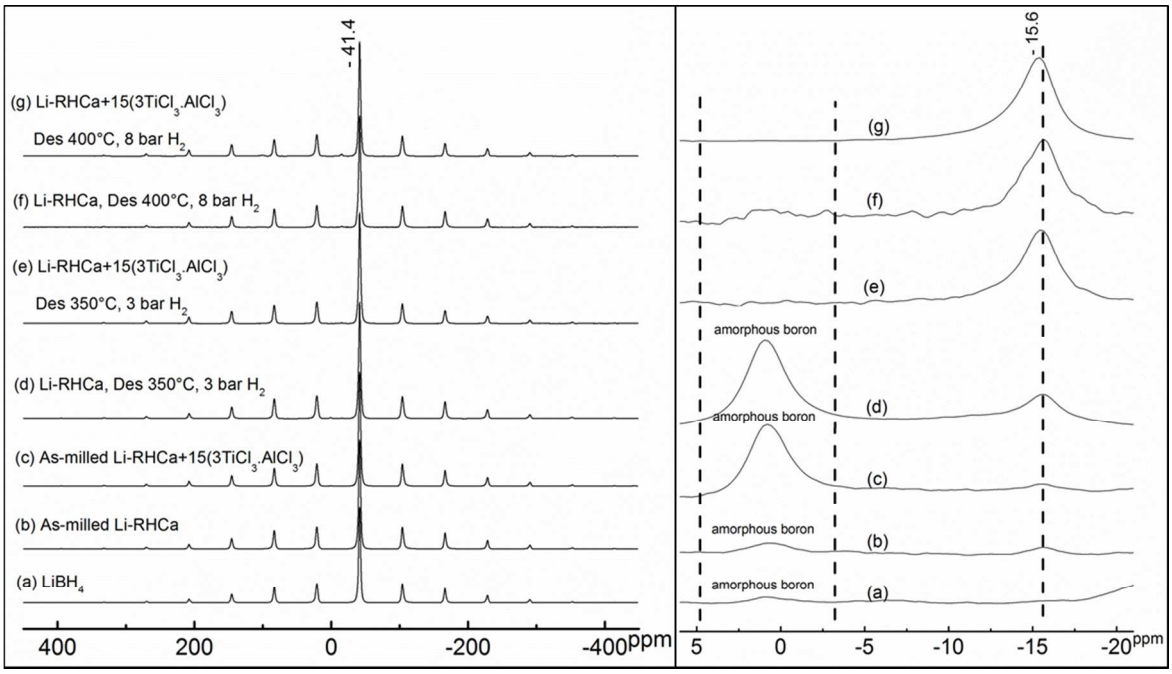

Figure 7. **A** NMR spectra of the (a) as-purchased $LiBH_4$, (b) as-milled Li-RHC_a, (b) as-milled Li-RHC_a+15($3TiCl_3.AlCl_3$), (d) Li-RHC_a partially dehydrogenated at 350 °C under 3 bar of H_2, (e) Li-RHC_a+15($3TiCl_3.AlCl_3$) partially dehydrogenated at 350 °C under 3 bar of H_2, (f) Li-RHC_a partially dehydrogenated at 400 °C under 8 bar of H_2, (g) Li-RHC_a+15($3TiCl_3.AlCl_3$) partially dehydrogenated at 400 °C under 8 bar of H_2. **B** Zoom of **A** between -20 to 5 ppm to

highlight the peaks belonging to $Li_2B_{12}H_{12}$ at about -15 ppm and amorphous boron between –2.5 ppm and 5 ppm.

Under these conditions, the equilibrium pressures of the reaction (8) (~1.5 bar H_2 at 350 °C and ~ 4 bar H_2 at 400 °C) and reaction (9) (~ 0.5 bar H_2 at 350 °C and ~ 1.5 bar H_2 at 400 °C) are below to the selected experimental pressures and hence reactions (8) and (9) can be avoided[10,14,57,58]. It is important to mention that the partially dehydrogenated samples have been taken from the reactor after the dehydrogenation of MgH_2 and after leaving the sample a while where no hydrogen release has been noticed.

The as-purchased $LiBH_4$, as-milled Li-RHC_a and as-milled Li-RHC_a+15($3TiCl_3.AlCl_3$) samples (Fig. 7A(a)-(c)) show strong signals of $LiBH_4$ at -41.4 ppm and broad peaks originating from amorphous boron. As seen in Fig. 7 B(a), as-purchased $LiBH_4$ contains just amorphous boron (besides $LiBH_4$). After milling (Fig. 7 B(b)), the as-milled Li-RHC_a also shows small and broad peaks that belong to $Li_2B_{12}H_{12}$. The addition of $3TiCl_3.AlCl_3$ during milling makes possible the formation of a larger amount of boron (Fig. 7 B(c) bigger area of the free boron peak) as a result of the formation of the AlTi alloys (mainly $AlTi_3$), which is in agreement with the predicted reaction (7) and the experimental results (ESI Fig. S4, S5 and Fig. 6). Therefore, this suggests that the energy transmitted by the grinding medium to the powder during milling is enough to promote two reactions. The first possible reaction is the decomposition of a small amount of $LiBH_4$ to free boron and $Li_2B_{12}H_{12}$ *via* two parallel reactions (reactions (8) and (9)). The second one is the reaction of the free boron contained in the as-purchased $LiBH_4$ with LiH stemming from the decomposition of $LiBH_4$ (as indicated in reaction (9)) to form $Li_2B_{12}H_{12}$ and more free boron. In the case of the as-milled Li-RHC_a after the partial dehydrogenation (Fig. 7 (d) and (f)), the presence of free boron (Fig. 7B(d)) and $Li_2B_{12}H_{12}$ is evident (Fig. 7 B(d) and (f)).

Experimental results show that during the first non-isothermal dehydrogenation of the as-milled Li-RHC_a the incubation period does not always last the same time (ESI Fig. S9). It implies that the incubation period related to the formation of $Li_2B_{12}H_{12}$ is highly dependent on the nature of the starting material and the amounts of boron and $Li_2B_{12}H_{12}$ generated during milling which seems not to be homogenously distributed in the material. For as-milled Li-RHC_a+15($3TiCl_3.AlCl_3$) after partial dehydrogenation (Fig. 7 B(e) and (g)), just the presence of $Li_2B_{12}H_{12}$ is noticed. Ohba *et al.*[10] has calculated that the decomposition of $Li_2B_{12}H_{12}$ towards LiH and free B presents a high enthalpy value of 125 kJ/mol H_2. Caputo *et al.*[12] based on first-principles calculations has reported that the decomposition of $LiBH_4$ can proceed *via* different pathways and proposed that the $Li_2B_{12}H_{12}$ is a product and not an intermediate phase because of its high stability. Pitt *et al.*[65] has experimentally confirmed that under vacuum or H_2 overpressure conditions anhydrous $Li_2B_{12}H_{12}$ begins to decompose after 250 °C to a substoichiometric $Li_2B_{12}H_{12-x}$ composition dependent on the amount of hydrogen released. Recently, White *et al.*[66] has shown that $Li_2B_{12}H_{12}$ can be converted into metal borides or borides species under harsh temperature and pressure conditions, e.g. the reaction between $Li_2B_{12}H_{12}$ and MgH_2 can form MgB_2 and LiH above 500 °C upon dehydrogenation in vacuum.

As mentioned above, the used temperature and hydrogen pressure conditions for the preparation of the samples for the NMR measurements (Fig. 7 (d)-(g)) are over the equilibrium pressures of reaction (8) and (9). In this regard and owing to the high stability of $Li_2B_{12}H_{12}$, it is possible to suggest that the small amount of formed $Li_2B_{12}H_{12}$ upon dehydrogenation can come from the reaction between LiH, generated during the formation of MgB_2, and the free boron contained in the as-purchased material and the one generated during the milling process. This analysis allows a thorough interpretation of the results shown in Fig. 1. For the first non-

isothermal dehydrogenation of Li-RHC_a at 400 °C under 3 bar of overpressure (Fig. 1 A(a)), the incubation period starts at about 400 °C. At these conditions, the equilibrium pressure of reaction (8) is about 4 bar and thus the reaction pathway can undergo to the slow formation of $Li_2B_{12}H_{12}$ and LiH with an insignificant hydrogen release. Moreover, the free boron, already contained in the as-purchased $LiBH_4$ material and then generated during milling, might react with the already formed LiH to produce more $Li_2B_{12}H_{12}$, which finally remains stable. The presence of $Li_2B_{12}H_{12}$ precludes the contact between free Mg and $LiBH_4$ and the fast formation of MgB_2. This process might retard the third step of the dehydrogenation (i.e. the reaction of $LiBH_4$ with Mg to form MgB_2) until a minimum amount of MgB_2 seeds are formed. In the case of the Li-RHC_a+x($3TiCl_3.AlCl_3$) (x = 7.5, 11, 15 and 30) (Fig. 1B), during milling the formation of nanosized $AlTi_3$ alloy (reaction (7)) produces free boron and $Li_2B_{12}H_{12}$ as by-products (Fig. 7 B(c)). Upon non-isothermal dehydrogenation (Fig. 1B(b)-(e)), a reduced incubation period (Li-RHC_a+7.5($3TiCl_3.AlCl_3$)) or the direct fast $LiBH_4$ decomposition (Li-RHC_a+11, 15, 30($3TiCl_3.AlCl_3$)) after the MgH_2 dehydrogenation are seen at about 400 °C under 3 bar H_2 of overpressure. The reaction (8) is partially or totally avoided. It is possible to infer that upon the first dehydrogenation the formation of stable $Li_2B_{12}H_{12}$ occurs as described for the as-milled Li-RHC_a. However, the well-distributed *in situ* formed nanosized $AlTi_3$ alloy acts as an efficient heterogeneous nucleation agent for the rapid formation of MgB_2 seeds (as shown in Section 4.3.1). In spite of the small amount of stable and irreversible $Li_2B_{12}H_{12}$, the availability of efficient heterogeneous nucleation sites improves the Mg-$LiBH_4$ contact and avoids the further generation of $Li_2B_{12}H_{12}$ by accelerating the formation of MgB_2. It is important to point out that in Fig. 2 and 3 the Li-RHC_a shows lower reversible hydrogen capacity and slightly higher deterioration rates than Li-RHC_d upon cycling. This fact may account for the presence of

amorphous boron in as-received $LiBH_4$ and to the further formation of stable $Li_2B_{12}H_{12}$ during milling.

4.3.3. Rate limiting step and hydrogenation-dehydrogenation activation energy

In order to elucidate if the notable kinetic enhancement (Fig. 3 and Fig. S1) of the Li-RHC_d+7.5($3TiCl_3.AlCl_3$) material is related to a change in the rate-limiting step and/or a decrease in the hydrogenation-dehydrogenation activation energy, gas-solid models have been applied.

Fig. 8A shows the hydrogenation kinetic curves of the second cycle at 390 °C and their respective model fittings for the Li-RHC_d+7.5($3TiCl_3.AlCl_3$) and Li-RHC_d materials. It is observed that the presence of the *in situ* formed AlTi alloys clearly increases the hydrogen uptake rate. In order to identify the proper rate limiting step mechanism for the hydrogenation process, the Sharp's and Jone's method has been applied: plotting the experimental value of $(t/t_{0.5})_{experimental}$ versus the theoretical ones $(t/t_{0.5})_{theoretical}$ (ESI Fig. S10)[67,68]. On the one hand, for all the hydrogenation curves of Li-RHC_d material in the range of temperature between 360 °C and 400 °C, the Johnson-Mehl-Avrami (JMA) reaction model with n= 1 (one dimensional interface-controlled reaction) is the most suitable one[69]. On the other hand, for the Li-RHC_d+7.5($3TiCl_3.AlCl_3$) material in the same range of temperature, the three-dimensional contracting volume reaction model (R3, three dimensional interface-controlled reaction) fits better[70]. Both models have been found as rate limiting steps in previous publications[25,64,71] (ESI Fig. S10). All hydrogenation curves show good fitting agreements with a correlation coefficient R^2 near 1 (Fig. 8A, ESI Fig. S11 kinetic curves fitting and fitting parameters for all the hydrogenation curves). *In-situ* SR-PXD measurements have shown that the hydrogenation process of the pure Li-RHC is a single step reaction which involves the formation of MgH_2 and

$LiBH_4$ from MgB_2 and LiH[17,24] and the same behavior has been observed in the *in situ* SR-PXD measurement carried out in this work (ESI Fig. S3). Fig. 8 (B and C) presents the hydrogenation activation energies (E_a) for the single step hydrogen uptake. As seen there, the hydrogenation E_a is reduced by about 60 kJ/mol H_2 due to the presence of the additive (Li-RHC_d = 184±6 kJ/mol H_2 and Li-RHC_d+7.5($3TiCl_3.AlCl_3$) = 124±6 kJ/mol H_2). The markedly improvement in the hydrogenation kinetic behavior can be attributed to two main factors: first, the reduced particle size of MgB_2 down to about 300 nm (ESI Fig. S7A) that leads to a faster MgB_2 consumption; second, the homogenous distribution of the nanosized particles of AlTi alloys located on the MgB_2 that prevents the agglomeration, generates more active surface for the hydrogen-material interaction and enables the faster three dimensional interface movement.

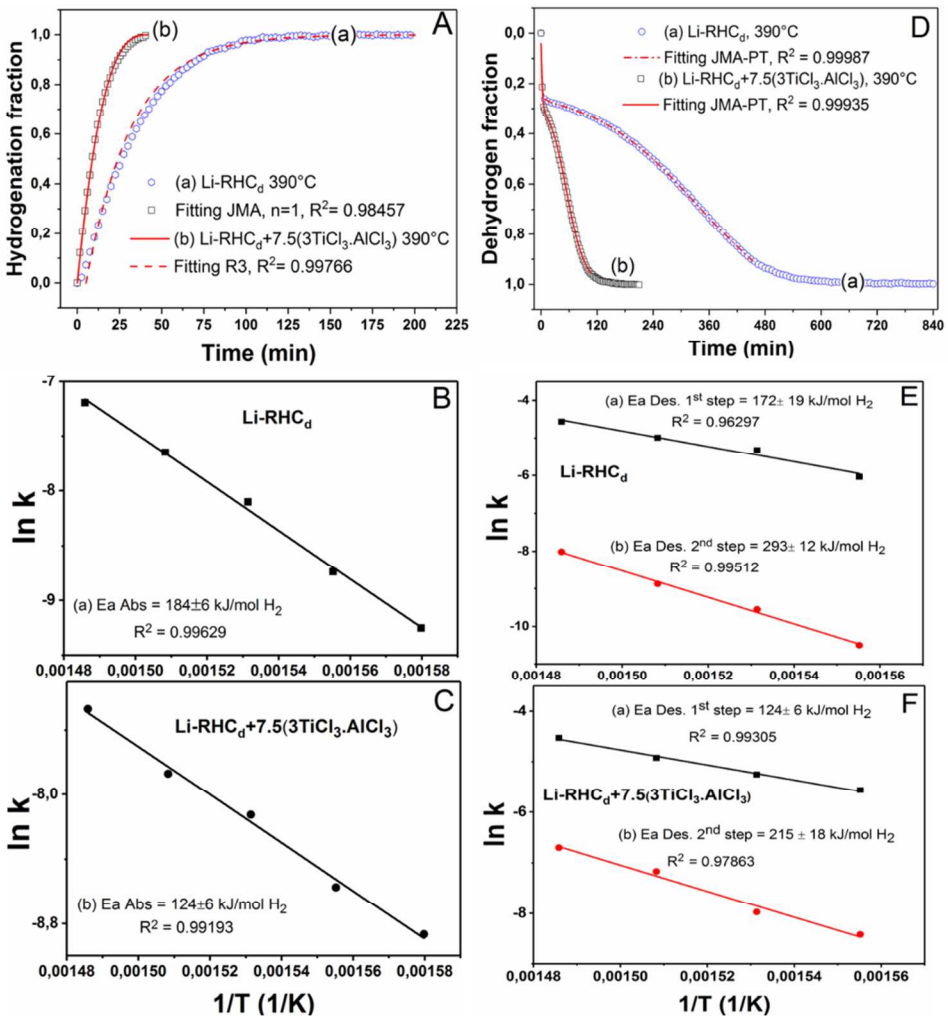

Figure 8. Kinetic behavior for Li-RHC$_d$ and Li-RHC$_d$+7.5(3TiCl$_3$.AlCl$_3$): **A** Hydrogenation and **D** Dehydrogenation kinetic curves of the 2nd cycle and model fitting. **B** and **C** Hydrogenation activation energy. **E** and **F** Dehydrogenation activation energy.

In Fig. 8D a comparison between the dehydrogenation kinetic curves of Li-RHC$_d$ and Li-RHC$_d$+7.5(3TiCl$_3$.AlCl$_3$) at 390 °C clearly shows that the doping improves notably the material's kinetic behavior. For the kinetic modelling of the dehydrogenation curves a novel approach proposed by Puszkiel *et al.*[64] has been applied, consisting in the combination of two kinetic models, i.e. the JMA model for the first step (MgH_2 decomposition) and the modified Prout-Topkins (PT) model for the second step (reaction between Mg and $LiBH_4$ to give LiH,

MgB_2 and H_2 release)[70,72]. The fitting employing the combined model[64] to the dehydrogenation curves of Li-RHC_d and Li-RHC_d+7.5($3TiCl_3.AlCl_3$) between 370 °C and 400 °C under 3 bar of H_2 shows good agreement with correlation coefficient R^2 of about 1 (Fig. 8D, ESI Fig. S12). During the first step of the dehydrogenation, the MgH_2 decomposition is limited by a MgH_2/Mg interface-controlled mechanism along a one-dimensional dislocation line (JMA with n ~ 1)[73]. Fig. 8 (E and F) exhibits the dehydrogenation E_a for Li-RHC_d and Li-RHC_d+7.5($3TiCl_3.AlCl_3$) corresponding to the first and second step. In the case of MgH_2 decomposition (Fig. 8E(a) and F(a)), E_a is decreased from 172±19 kJ/mol H_2 for Li-RHC_d to 124±6 kJ/mol H_2 for Li-RHC_d+7.5($3TiCl_3.AlCl_3$). These results suggest that the reaction kinetics of the first step of the dehydrogenation process for Li-RHC_d is enhanced by the presence of the nanosized AlTi alloy, which has been already seen for pure MgH_2[73]. Fig.8 E(b) and F(b) show the dehydrogenation E_a belonging to the second step for Li-RHC_d and Li-RHC_d+7.5($3TiCl_3.AlCl_3$), respectively. The dehydrogenation E_a for Li-RHC_d+7.5($3TiCl_3.AlCl_3$) is lower than that for Li-RHC_d, i.e. 215±18 kJ/mol H_2 and 293±12 kJ/mol H_2, respectively. This is in agreement with the fitted autocatalytic (PT) model, in which the involvement of products as reactive phases is considered[70]. As explained in a previous section (4.3.1), the interaction of $3TiCl_3.AlCl_3$ with the Li-RHC material produces *in situ* nanosized AlTi alloys. Hexagonal $AlTi_3$ is the most abundant nanosized AlTi phase. This phase presents excellent properties to promote the fast growth of MgB_2 nuclei and it is very well distributed. Therefore, the dehydrogenation E_a of the second step is markedly reduced due to the availability of well-distributed hexagonal $AlTi_3$ nanoparticles acting as effective nucleation centers and allowing the fast formation of MgB_2 on their surfaces.

5. CONCLUSIONS

In this work, the effect of the formation of nano TiAl alloys on the hydrogenation storage properties of the $2LiBH_4+MgH_2/2LiH+MgB_2$ system has been investigated in detail. The samples have been prepared in both hydrogenated and dehydrogenated states adding either $3TiCl_3.AlCl_3$ or $TiCl_3$. The hydrogenation/dehydrogenation rates of the doped composite systems show a significant enhancement compared to the pristine material. The $7.5(3TiCl_3.AlCl_3)$ doped Li-RHC_d exhibits the best performance among the investigated systems. In fact, for this material the hydrogenation-dehydrogenation times are about 30 minutes and the reversible hydrogen storage capacity is about 9.5 wt.%. These values are stable through 20 hydrogenation/dehydrogenation cycles. Moreover, in comparison to the pristine material, the activation energy for the hydrogenation of the Li-RHC_d+$7.5(3TiCl_3.AlCl_3)$ is significantly reduced by 60 kJ/mol H_2. The dehydrogenation activation energies of the first and the second steps are also considerably decreased by about 50 kJ/mol H_2 and 80 kJ/mol H_2, respectively. This shows that the addition of $3TiCl_3.AlCl_3$ has a strong effect on the Li-RHC system and a beneficial effect by avoiding the further generation of $Li_2B_{12}H_{12}$. It has been found that the nanosized AlTi alloys are formed *in situ* as a result of the interaction between the $3TiCl_3.AlCl_3$ additive and Li-RHC upon milling. Among the observed AlTi alloys, the nanosized hexagonal $AlTi_3$ is the most abundant species. These AlTi nanoparticles are stable upon hydrogenation/dehydrogenation cycling. The enhanced hydrogenation kinetic behavior is attributed to the nanosized AlTi alloys which facilitates the reduction of the particle size of MgB_2 down to about 300 nm leading to a faster MgB_2 consumption, preventing the MgB_2 agglomeration, generating more active surface for the hydrogen-material interaction and making possible the faster three dimensional interface movements. Upon dehydrogenation, nanosized AlTi alloys also account for the improvement during the first and second dehydrogenation steps.

The decomposition of MgH_2 during the first step is catalyzed by the presence of these well-distributed nanosized AlTi alloys. Furthermore, the kinetic behavior during second dehydrogenation step is improved by the presence of *in situ* formed nanosized and hexagonal $AlTi_3$, which acts as an effective heterogeneous nucleation site for MgB_2 nuclei and precludes the additional formation of $Li_2B_{12}H_{12}$. This novel catalytic mechanism opens a potential for an economical and efficient design of hydrogen storage materials.

ASSOCIATED CONTENT

Supporting Information. Hydrogenation-dehydrogenation curves during 20 cycles of tested materials, coupled Sieverts-DSC measurements of the undoped and doped Li-RHC samples, *in situ* SR-PXD data of a full sorption process of the Li-RHC_d+7.5($3TiCl_3.AlCl_3$) sample, *ex situ* PXD of the doped samples prepared in the hydrogenated state Li-RHC_a+7.5($3TiCl_3.AlCl_3$) after milling and after cycling, *in situ* SR-PXD data of the desorption reaction measured for the sample Li-RHC_a+7.5($3TiCl_3.AlCl_3$) after milling, ASAXS curves of the as-milled Li-RHC_d+7.5$TiCl_3$ sample, thermodynamic data parameters for thermodynamic calculations, EDS/STEM mode of Li-RHC_d+7.5($3TiCl_3.AlCl_3$) after milling and after cycling, HR-TEM micrographs of Li-RHC_d+7.5($3TiCl_3.AlCl_3$), first non-isothermal dehydrogenation of as-milled Li-RHC_a, $(t/t0.5)_{experimental}$ vs. $(t/t0.5)_{theoretical}$ plots for Li-RHC_d and Li-RHC_d+7.5($3TiCl_3.AlCl_3$), Li-RHC_d and Li-RHC_d+7.5($3TiCl_3.AlCl_3$) hydrogenation and dehydrogenation curves fitted in the range of temperature between 360 ^oC and 400 ^oC.

AUTHOR INFORMATION

Corresponding Author

* E-mail: claudio.pistidda@hzg.de, Tel: +49 (0)4152 87-2644

Author Contributions

All authors have given approval to the final version of the manuscript.

Notes

The authors declare no competing financial interest.

ACKNOWLEDGEMENTS

This research was supported by the European Marie Curie Actions under ECOSTORE grant agreement number 607040 and by ANPCyT – (Agencia Nacional de Promoción Científica y Tecnológica) - PICT 2015 1865. The authors gratefully acknowledge support from The Danish National Research Foundation, Center for Materials Crystallography (DNRF93), The Innovation Fund Denmark (HyFill-Fast), and by the Danish Research Council for Nature and Universe (Danscatt). The authors also thank CONICET (Consejo Nacional de Invetigaciones Científicas y Técnicas), ANPCyT – (Agencia Nacional de Promoción Científica y Tecnológica), CNEA (Comisión Nacional de Energía Atómica), HZB-BESSY II Laboratory (Proposal ID: 20140433), Dr. Anna-Lisa Chaudhary (Helmholtz-Zentrum Geesthacht).

REFERENCES

(1) Jepsen, L.; Ley, M. B.; Lee, Y. S.; Cho, Y. W.; Dornheim, M.; Jensen, J. O.; Filinchuk, Y.; Jørgensen, J. E.; Besenbacher, F.; Jensen, T. R. Boron-Nitrogen based Hydrides and Reactive Composites for Hydrogen Storage. *Mater. Today* **2014**, *17*, 129-135.

(2) Ley, M. B.; Jepsen, L. H.; Lee, Y. S.; Cho, Y. W.; Bellosta von Colbe, J.; Dornheim, M.; Rokni, M.; Jensen, J. O.; Sloth, M.; Filinchuk, Y.; et al. Complex Hydrides for Hydrogen Storage – New Perspectives. *Mater. Today* **2014**, *17*, 122-128.

(3) Broom, D. P. *Hydrogen Storage Materials*: *The Characterisation of Their Storage Properties*. Springer, London, 2011.

(4) Callini, E.; Atakli, Z. Ö. K.; Hauback, B. C.; Orimo, S.; Jensen, C.; Dornheim, M.; Grant, D.; Cho, Y. W.; Chen, P.; Hjörvarsson, B.; et al. Complex and Liquid Hydrides for Energy Storage. *Appl. Phys. A* **2016**, *122:353*, 1-22.

(5) Møller, K. T.; Jensen, T. R.; Akiba, E.; Li, H.-W. Hydrogen - A Sustainable Energy Carrier. *Progress in Natural Science: Materials International* **2017**, *27*, 34-40.

(6) Züttel, A.; Wenger, P.; Rentsch, S.; Sudan, P.; Mauron, Ph.; Emmenegger, C. $LiBH_4$ a New Hydrogen Storage Material. *J. Power Sources* **2003**, *118*, 1-7.

(7) Paskevicius, M.; Jepsen, L. H; Schouwink, P.; Černý, R.; Ravnsbæk, D. B.; Filinchuk Y.; Dornheim, M.; Besenbacher, F.; Jensen, T. R. Metal Borohydrides and Derivatives Synthesis, Structure and Properties. *Chem. Soc. Rev.* **2017**, *46*, 1565-1634.

(8) Puszkiel, J. A.; Garroni, S.; Milanese, C.; Gennari, F.; Klassen, T.; Dornheim, M.; Pistidda, C. Tetrahydroborates: Development and Potential as Hydrogen Storage Medium. *Inorganics* **2017**, *5*, 1-24.

(9) Orimo, S. I.; Nakamori, Y.; Ohba, N.; Miwa, K.; Aoki, M.; Towata, S.; Züttel, A. Experimental Studies on Intermediate Compound of $LiBH_4$. *Appl. Phys. Lett.* **2006**, *89*, 021920.

(10) Ohba, N.; Miwa, K.; Aoki, M.; Noritake, T.; Towata S. I.; Nakamori, Y.; Orimo, S. I.; Züttel, A. First-Principles Study on the Stability of Intermediate Compounds of $LiBH_4$. *Phys. Rev. B – Condens. Matter Mater. Phys.* **2006**, *74*, 075110.

(11) Hwang, S. J.; Bowman, R. C.; Reiter, J. W.; Rijssenbeek, J.; Soloveichik, G. L.; Zhao, J. C.; Kabbour, H.; Ahn, C. C. NMR Confirmation for Formation of $[B_{12}H_{12}]^{2-}$ Complexes

during Hydrogen Desorption from Metal Borohydrides. *J. Phys. Chem. C* **2008**, *112*, 3164–3169.

(12) Caputo, R.; Züttel, A. First-Principles Study of the Paths of the Decomposition Reaction of $LiBH_4$. *Mol. Phys.* **2010**, *108*, 1263-1276.

(13) Friedrichs, O.; Remhof, A.; Hwang, S. J.; Züttel, A. Role of $Li_2B_{12}H_{12}$ for the Formation and Decomposition of $LiBH_4$. *Chemistry of Materials* **2010**, *22*, 3265-3268.

(14) Mauron, P.; Buchter, F.; Friedrichs, O.; Remhof, A.; Bielmann, M.; Zwicky, C. N.; Züttel, A. Stability and Reversibility of $LiBH_4$. *J. Phys. Chem. B* **2008**, *112*, 906-910.

(15) Barkhordarian, G.; Klassen, T.; Dornheim, M.; Bormann, R. Unexpected Kinetic Effect of MgB_2 in Reactive Hydride Composites Containing Complex Borohydrides. *J. Alloys and Compd.* **2007**, *440*, L18-L21.

(16) Vajo, J. J.; Skeith, S. L. Reversible Storage of Hydrogen in Destabilized $LiBH_4$. *J. Phys. Chem. B* **2005**, *109*, 3719-3722.

(17) Bösenberg, U.; Doppiu, S.; Mosegaard, L.; Barkhordarian, G.; Eigen, N.; Borgschulte, A.; Jensen, T. R.; Cerenius, Y.; Gutfleisch, O.; Klassen, T.; et al. Hydrogen Sorption Properties of MgH_2-$LiBH_4$ Composites. *Acta Mater.* **2007**, *55*, 3951-3958.

(18) Pistidda, C.; Garroni, S.; Bonatto Minella, C.; Dolci, F.; Jensen, T. R.; Nolis, P.; Bösenberg, U.; Cerenius, Y.; Lohstroh, W.; Fichtner, M.; et al. Pressure Effect on the $2NaH + MgB_2$ Hydrogen Absorption Reaction. *J. Phys. Chem. C* **2010**, *114*, 21816–21823.

(19) Bonatto Minella, C.; Garroni, S.; Olid, D.; Teixidor, F.; Pistidda, C.; Lindemann, I.; Gutfleisch, O.; Baro, M. D.; Bormann, R.; Klassen, T.; et al. Experimental Evidence of

$Ca[B_{12}H_{12}]$ Formation During Decomposition of a $Ca(BH_4)_2$ + MgH_2 based Reactive Hydride Composite. *J. Phys. Chem. C* **2011**, *115*, 18010-18014.

(20) Karimi, F.; Pranzas, P. K.; Pistidda, C.; Puszkiel, J. A.; Milanese, C.; Vainio, U.; Paskevicius, M.; Emmler, T.; Santoru, A.; Utke, R.; et al. Structural and Kinetic Investigation of the Hydride Composite $Ca(BH_4)_2$ + MgH_2 System doped with NbF_5 for Solid-State Hydrogen Storage. *Phys. Chem. Chem. Phys.* **2015**, *17*, 27328-27342

(21) Karimi, F.; Pranzas, P. K.; Hoell, A.; Vainio, U.; Welter, E.; Raghuwanshi, V. S.; Pistidda, C.; Dornheim, M.; Klassen, T.; Schreyer, A. Structural Analysis of Calcium Reactive Hydride Composite for Solid State Hydrogen Storage. *J. Appl. Crystallogr*. **2014**, *47*, 67-75.

(22) Minella, C. B.; Pistidda, C.; Garroni, S.; Nolis, P.; Baró, M. D.; Gutfleisch, O.; Klassen, T.; Bormann, R.; Dornheim, M. $Ca(BH_4)_2$ + MgH_2: Desorption Reaction and Role of Mg on Its Reversibility. *J. Phys. Chem. C* **2013**, *117*, 3846-3852.

(23) Pinkerton, F. E.; Martin, M. S.; Meisner, G. P.; Balogh, M. P.; Vajo, J. J. Phase Boundaries and Reversibility of $LiBH_4/MgH_2$ Hydrogen Storage Material. *J. Phys. Chem. C* **2007**, *111*, 12881-12885.

(24) Bösenberg, U.; Ravnsbæk, D. B.; Hagemann, H.; D'Anna, V.; Bonatto Minella, C.; Pistidda, C.; Beek, W. V.; Jensen, T. R.; Bormann, R.; Dornheim, M. Pressure and Temperature Influence on the Desorption Pathway of the $LiBH_4$–MgH_2 Composite System. *J. Phys. Chem. C* **2010**, *114*, 15212-15217.

(25) Bösenberg, U.; Kim, J. W.; Gosslar, D.; Eigen, N.; Jensen, T. R.; Bellosta von Colbe, J. M.; Zhou, Y.; Dahms, M.; Kim, D. H.; Günther, R.; et al. Role of Additives in $LiBH_4$–MgH_2 Reactive Hydride Composites for Sorption Kinetics. *Acta Mater.* **2010**, *58*, 3381–3389.

(26) Deprez, E.; Munoz-Marquez, M. A.; Roldan, M. A.; Prestipino, C.; Palomares, F. J.; Bonatto Minella, C.; Bösenberg, U.; Dornheim, M.; Bormann, R.; Fernandez, A. Oxidation State and Local Structure of Ti-based Additives in the Reactive Hydride Composite $2LiBH_4$-MgH_2. *J. Phys. Chem. C* **2010**, *114*, 3309-3317.

(27) Fan, M. Q.; Sun, L. X.; Zhang, Y.; Xu, F.; Zhang, J.; Chu, H. L. The Catalytic Effect of Additive Nb_2O_5 on the Reversible Hydrogen Storage Performances of $LiBH_4$-MgH_2 Composite. *Int. J. Hydrogen Energy* **2008**, *33*, 74-80.

(28) Deprez, E.; Justo, A.; Rojas, T. C.; Lo´pez-Carte´s, C.; Bonatto Minella, C.; Bösenberg, U.; Dornheim, M.; Bormann, R.; Fernandez, A. Microstructural Study of the $LiBH_4$-MgH_2 Reactive Hydride Composite with and without Ti-isopropoxide Additive. *Acta. Mater.* **2010**, *58*, 5683-5694.

(29) Wang, P.; Ma, L.; Fang, Z.; Kang, X.; Wang, P. Improved Hydrogen Storage Property of Li-Mg-B-H System by Milling with Titanium Trifluoride. *Energy Environ. Sci.* **2009**, *2*, 120-123.

(30) Kou, H. Q.; Sang, G.; Zhou, Y. L.; Wang, X. Y.; Hu. C. Q. Enhanced Hydrogen Storage Properties of $LiBH_4$ Modified by NbF_5. *Int. J. Hydrogen Energy* **2014**, *39*, 11675-11682

(31) Sridechprasat, P.; Suttisawat, Y.; Rangsunvigit, P.; Kitiyanan, B.; Kulprathipanja, S. Catalyzed $LiBH_4$ and MgH_2 Mixture for Hydrogen Storage. *Int. J. Hydrogen Energy* **2011**, *36*, 1200-1205.

(32) Li, Y.; Izuhara, T.; Takeshita, H. T. Promotional Effect of Aluminum on MgH_2+$LiBH_4$ Hydrogen Storage Materials: Special Issue on Advanced Materials for Hydrogen Energy Applications. *Materials Transactions* **2011**, *52*, 641-646.

(33) Liu, B. H.; Zhang, B. J.; Jiang, Y. Hydrogen Storage Performance of $LiBH_4$+1/2MgH_2 Composites Improved by Ce-based Additives. *Int. J. Hydrogen Energy* **2011**, *36*, 5418-5424.

(34) Bösenberg, U.; Vainio, U.; Pranzas, P. K.; Bellosta von Colbe, J. M.; Goerigk, G.; Welter, E.; Dornheim, M.; Schreyer, A.; Bormann, R. On the Chemical State and Distribution of Zr- and V-based Additives in Reactive Hydride Composites. *Nanotechnology* **2009,** *20*, 204003.

(35) Cerenius, Y.; Staal, K.; Svensson, L. A.; Usby, T.; Oskasson, A.; Albertson, J.; Liljas, A. The Crystallography Beamline I711 at MAX II. *J. Synchrotron Radiat.* **2000**, *7*, 203-208.

(36) Bösenberg, U.; Pistidda, C.; Tolkiehn, M.; Busch, N.; Saldan, I.; Suarez-Alcantara, K.; Arendarska, A.; Klassen, T.; Dornheim, M. Characterization of Metal Hydrides by In-situ XRD. *Int. J. Hydrogen Energy* **2014**, *39*, 9899-9903.

(37) Pistidda, C.; Santoru, A.; Garroni, S.; Bergemann, N.; Rzeszutek, A.; Horstmann, C.; Thomas, D.; Klassen, T.; Dornheim, M. First Direct Study of the Ammonolysis Reaction in

the Most Common Alkaline and Alkaline Earth Metal Hydrides by In-situ SR-PXD. *J. Phys. Chem. C* **2015**, *119*, 934-943.

(38) Hammersley, A.P. FIT2D: An Introduction and Overview, ESRF Internal Report, ESRF97HA02T **1997**.

(39) Krumrey, M. Design of a Four-Crystal Monochromator Beamline for Radiometry at BESSY II. *J. Synchrotron Radiat.* **1998**, *5*, 6-9.

(40) Bieder, H.; Hoell, A.; Mokrani, L.; Zizak, I. Patent DE102006029449. **2007**.

(41) Krumrey, M.; Ulm, G. High-Accuracy Detector Calibration at the PTB Four-Crystal Monochromator Beamline. *Nucl. Instr. and Meth. In Phys. Res. A* **2001**, *467–468*, 1175-1178.

(42) Wernecke, J.; Gollwitzer, C.; Müller, P.; Krumrey, M. Characterization of an In-Vacuum PILATUS 1M Detector. *J. Synchrotron. Radiat.* **2014**, *21*, 529-536.

(43) Hoell, A.; Tatchev, D.; Haas, S.; Haug, J.; Boesecke, P. On the Determination of Partial Structure Functions in Small-Angle Scattering Exemplified by $Al_{89}Ni_6La_5$ Alloy. *J. Appl. Crystallogr.* **2009**, *42*, 323-325.

(44) Cromer, D. T.; Liberman, D. Relativistic Calculation of Anomalous Scattering Factors for X Rays. *J. Chem. Phys.* **1970**, *53*, 1891-1987.

(45) Haas, S.; Hoell, A.; Zehl, G.; Dorbandt, I.; Bogdanoff, P.; Fiechter, S. Structural Investigation of Carbon Supported Ru-Se Based Catalysts Using Anomalous Small Angle X-Ray Scattering. *ECS Transactions* **2008**, *6*, 127-138.

(46) Breβler, I.; Kohlbrecher, J.; Thünemann. A. F. SASfit: A Tool for Small-Angle Scattering Data Analysis using a Library of Analytical Expressions. *J. Appl. Crystallogr.* **2015**, *48*, 1587-1598.

(47) Outokumpu HSC Chemistry for Windows, version 6.0, Outokumpu Research Oy, Pori, Finland, **2009**.

(48) Jepsen, J. Technical and Economic Evaluation of Hydrogen Storage Systems based on Light Metal Hydrides. Ph.D Thesis, Helmut Schmidt University, Hamburg, Germany, **2014**.

(49) Sigma Aldrich. http://www.sigmaaldrich.com/catalog (assessed Jan 18, 2017)

(50) Alfa Aesar. https://www.fishersci.de/shop/products/titanium-iii-chloride-aluminum-iii-chloride-ticl3-76-0-78-5-alfa-aesar-1/11314257#?keyword=TiCl3 (assessed Jan 18, 2017)

(51) Fedneva, E.M.; Alpatova, V.L.; Mikheeva, V.I. Thermal Stability of Lithium Borohydride. *Transl. Zh. Neorg. Khim. Russ. J. Inorg. Chem*. **1964**, *9*, 826–827.

(52) Nakagawa, T.; Ichikawa, T.; Hanada, H.; Kojima, Y.; Fujii, H. Thermal Analysis on the Li–Mg–B–H Systems. *J. Alloys and Compd.* **2007**, *446-447*, 306-309.

(53) Pranzas, P. K.; Bösenberg, U.; Karimi, F.; Münning, M.; Metz, O.; Bonatto Minella, C.; Schmitz, H. W.; Beckmann, F.; Vainio, U.; Zajac, D.; et al. Characterization of Hydrogen Storage Materials and Systems with Photons and Neutrons. *Adv. Eng. Mater.* **2011**, *13*, 730-736.

(54) Zhang, M. X.; Kelly, P. M. Edge-to-Edge Matching Model for Predicting Orientation Relationships and Habit Planes-The Improvements. *Script. Mater.* **2005**, *52*, 963–968.

(55) Bonatto Minella, C.; Pellicer, E.; Rossinyol, E.; Karimi, F.; Pistidda, C.; Garroni, S.; Milanese, C.; Nolis, P.; Baro, M. D.; Gutfleisch, O.; et al. Chemical State, Distribution, and Role of Ti- and Nb-Based Additives on the $Ca(BH_4)_2$ System. *J. Phys. Chem. C* **2013**, *117*, 4394−4403.

(56) Yan, Y.; Li, H. W.; Maekawa, H.; Miwa, K.; Towata, S.; Orimo, S. Formation of Intermediate Compound $Li_2B_{12}H_{12}$ during the Dehydrogenation Process of the $LiBH_4$–MgH_2 System. *J. Phys. Chem. C* **2011**, *115*, 19419-19423.

(57) Kim, K. B.; Shim, J. H.; Park, S. H.; Choi, I. S.; Oh, K. H.; Cho, Y. W. Dehydrogenation Reaction Pathway of the $LiBH_4$–MgH_2 Composite under Various Pressure Conditions. *J. Phys. Chem. C* **2015**, *119*, 9714-9720.

(58) Puszkiel, J.; Castro Riglos, M. V.; Karimi, F.; Santoru, A.; Pistidda, C.; Klassen, T.; Bellosta von Colbe, J. M.; Dornheim, M. Changing the Dehydrogenation Pathway of $LiBH_4$–MgH_2 via Nanosized Lithiated TiO_2. *Phys. Chem. Chem. Phys.* **2017**, *19*, 7455-7460.

(59) Kim, K. B.; Shim, J. H.; Oh, K. H.; Cho, Y. W. Role of Early-Stage Atmosphere in the Dehydrogenation Reaction of the $LiBH_4$–YH_3 Composite. *J. Phys. Chem. C* **2013**, *117*, 8028-8031.

(60) Kim, K. B.; Shim, J. H.; Cho, Y. W; Oh, K. H. Pressure-Enhanced Dehydrogenation Reaction of the $LiBH_4$–YH_3 Composite. *Chem. Com.* **2011**, *47*, 9831-9833.

(61) Kostka, J.; Lohstroh, W.; Fichtner. M; Hahn, H. Diborane Release from $LiBH_4$/Silica-Gel Mixtures and the Effect of Additives. *J. Phys. Chem. C* **2007**, *111*, 14026-14029.

(62) Friedrichs, O.; Remhof, A.; Hwang, S. J.; Züttel, A. Role of $Li_2B_{12}H_{12}$ for the Formation and Decomposition of $LiBH_4$. *Chemistry of Materials* **2010**, *22*, 3265-3268.

(63) Shao, H.; Felderhoff, M.; Weidenhalter, C. Kinetics Enhancement, Reaction Pathway Change, and Mechanism Clarification in $LiBH_4$ with Ti-Catalyzed Nanocrystalline MgH_2 Composite. *J. Phys. Chem. C* **2015**, *119*, 2341-2348.

(64) Puszkiel, J.; Castro Riglos, M. V.; Ramallo-López, J. M.; Mizrahi, M.; Karimi, F.; Santoru, A.; Hoell, A.; Gennari, F. C.; Arneodo Larochette, P.; Pistidda, C.; et al. A Novel Catalytic Route for Hydrogenation–Dehydrogenation of 2LiH + MgB_2 *via* In-situ formed Core–Shell Li_xTiO_2 Nanoparticles. *J. Mater. Chem. A* **2017**, *5*, 12922-12933.

(65) Pitt, M. P.; Paskevicius, M.; Brown, D. H.; Sheppard, D. A.; Buckley. C. E. Thermal Stability of $Li_2B_{12}H_{12}$ and its Role in the Decomposition of $LiBH_4$. *J. Am. Chem. Soc.* **2013**, *135*, 6930–6941.

(66) White, J. L.; Newhouse, R. J.; Zhang, J. Z.; Udovic, T. J.; Stavila, V. Understanding and Mitigating the Effects of Stable Dodecahydro-closo-dodecaborate Intermediates on Hydrogen-Storage Reactions. *J. Phys. Chem. C* **2016**, *120*, 25725–25731

(67) Sharp, J. H.; Brindley, G. W.; Narahari Achar, B. N. Numerical Data for Some Commonly used Solid State Reaction Equations. *J. Am. Ceram. Soc.* **1966**, *49*, 379-382.

(68) Jones, L. F.; Dollimore, D.; Nicklim, T. Comparison of Experimental Kinetic Decomposition Data with Master Data using a Linear Plot Method. *Thermochim. Acta* **1975**, *13*, 240-245.

(69) Christian, J. W. *The Theory of Transformations in Metals and Alloys*. 3rd ed. Amsterdam: Pergamon, **2002**.

(70) Khawam, A.; Flanagan, D. R. Solid-State Kinetic Models: Basics and Mathematical Fundamentals. *J. Phys. Chem. B* **2006**, *110*, 17315–17328.

(71) Puszkiel, J.; Gennari, F. C.; Arneodo Larochette, P.; Ramallo-López, J. M.; Vainio, U.; Karimi, F.; Pranzas, P. K.; Troiani, H.; Pistidda, C.; Jepsen, J.; et al. Effect of Fe Additive on the Hydrogenation-Dehydrogenation Properties of $2LiH + MgB_2/2LiBH_4 + MgH_2$ System. *J. Power Sources* **2015**, *284*, 606-616.

(72) Brown, M. E. The Prout-Tompkins Rate Equation in Solid-State Kinetics. *Thermochim. Acta* **1997**, *300*, 93-106.

(73) Wang, Y.; An, C.; Wang, Y.; Huang, Y.; Chen, C.; Jiao, L.; Yuan, H. Core–Shell Co@C Catalyzed MgH_2: Enhanced Dehydrogenation Properties and its Catalytic Mechanism. *J. Mater. Chem. A* **2014**, *2*, 16285-16291.

TOC Graphic